

Ultralow thermal conductivity and mechanical resilience of architected nanolattices.

ROB JAGT (s1910744), MSc APPLIED PHYSICS

Colaborator: Nicholas Dou

Supervisors: Prof. Julia R. Greer, Prof. Austin J. Minnich, Prof. Jeff Th. M. de Hosson
University of Groningen, May 2017

Abstract

The use of architecture in nanoarchitected material enables the independent manipulation of coupled physical attributes and the development of materials with unprecedented capabilities. Ceramics have some of the highest strength- and stiffness-to-weight ratios of any material and have intrinsically low thermal conductivity, but are suboptimal for use as structural materials because of their brittleness and sensitivity to flaws. Here it is demonstrated that the creation of structural metamaterials composed of nanoscale ceramics can create materials which are simultaneously ultralight, strong, thermally insulating and mechanically resilient, meaning that it can recover its original shape after compressions in excess of 50% strain. The measured combination of specific modulus (stiffness divided by density) and thermal conductivities have not been found in any other material. Further decoupling of mechanical and thermal properties for specific materials could be achieved by using classical size effects present in thin films.

CONTENTS

I	Introduction	4
II	Theory	8
I	Mechanical properties of nanolattices	8
II	Thermal properties of nanolattices	9
III	Determining the thermal conductivity of nanolattices	14
IV	Mechanical properties of nanolattices	15
III	Experimental setup	16
I	Temperature measurement	16
II	3ω experiment.	18
III	Mechanical compression experiments	20
IV	Sample fabrication	20
I	Writing structures using two photon lithography	20
II	Thin deposition techniques	22
III	Hollowing out structures	23
IV	Gold deposition onto structures	24
V	Microfabrication	25
VI	Creating the top plate	27
VII	Final result	29
V	Results	30
I	Validation on Glass	30
II	Thermal conductivity of polymer nanolattices	31
III	Thermal conductivity of alumina nanolattices	33
IV	Thermal conductivity of silicon nanolattices	33
V	Mechanical properties of alumina nanolattices	33
VI	Multifunctional properties of alumina nanolattices	36
VI	Discussion	38
I	Breakdown of the 1D heat transport assumption	39
II	Influence of non-ideal electronics	39
III	Presence of size effects	42
IV	Discussion on the mechanical data	44
V	Other methods to determine the thermal conductivity	45
VII	Future work	45
I	Using the concept of architecture to alter material properties	46
II	Decoupling thermal and other material properties	46
VIII	Conclusions	49
IX	Supplementary	50
X	Acknowledgment	52

I. INTRODUCTION

When one wants to determine the properties of a specific material, most of its properties can be understood by knowing the constituent features of the material at the microscale. This specific microstructure depends on the composition of the material and generally is the result of the way the material is synthesized and processed. The understanding of these *structure* \rightarrow *processing* \rightarrow *properties* relationships is generally known as the materials paradigm and is very important in the field of material science.

These micro structural features govern the *intrinsic* material properties. I.e. given a specific micro structure one can tabulate its material properties and it is assumed that these material properties are constant throughout the bulk. However next to the intrinsic characteristic microstructural length scale the external dimensions of the material system may also play a role. For example consider figure 1.

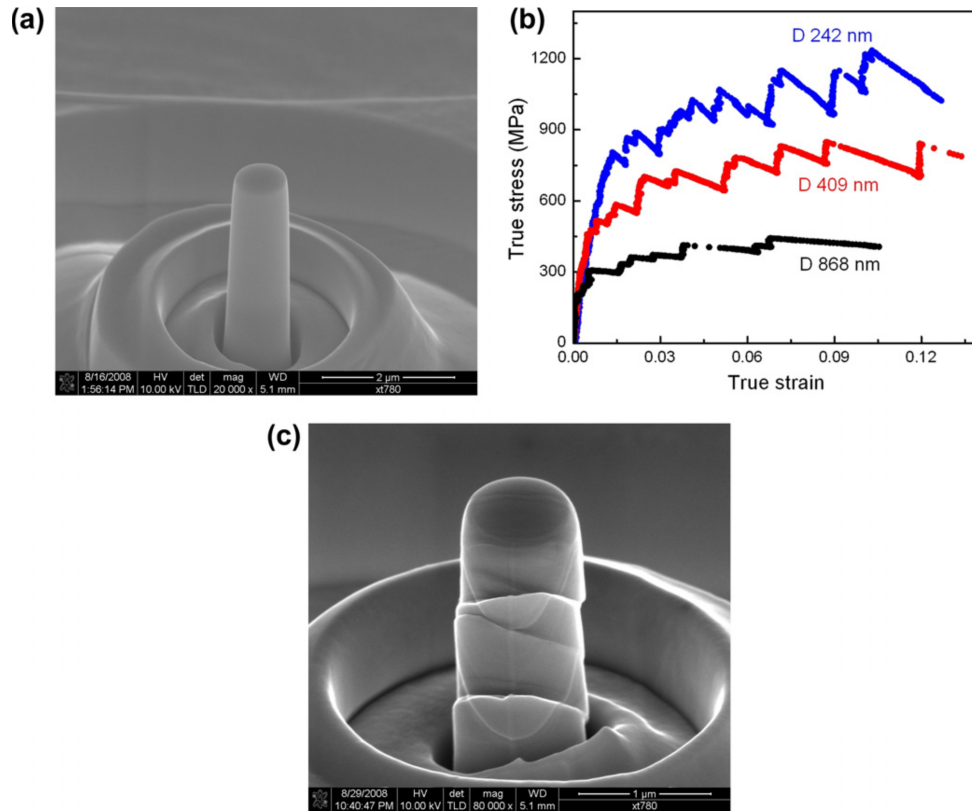


Figure 1: SEM images of a 800 nm diameter single crystalline Nb nano-pillar before (a) and after (c) of single crystalline Nb nanopillars with different diameters shown above each curve. (b) compression accompanied by compressive stress versus strain curves. Taken from 2.

Here an SEM image of a single crystalline Nb nano pillar before and after compression are shown together with the stress versus strain data of a pillar compression test for three different pillar diameters 2. What is apparent from the stress versus strain curves is that the pillars with smaller diameter becomes stronger. This is caused by annihilation of the initial mobile dislocations at

the free surface. The shear flow stress normalized by the shear modulus on the appropriate slip system for most face-centered cubic (fcc) metallic micro- and nano-pillars tested in compression and tension are depicted in figure 2.

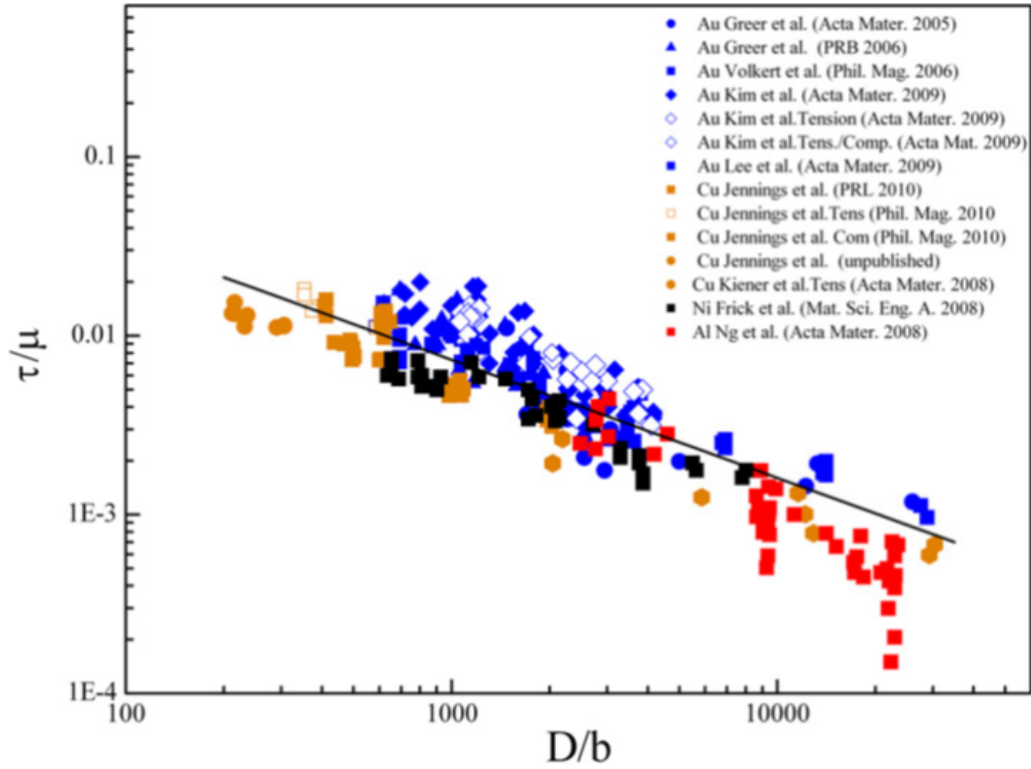


Figure 2: The shear flow stress normalized by the shear modulus on the appropriate slip system for most face-centered cubic (fcc) metallic micro- and nano-pillars tested in compression and tension. Taken from 3.

As can be seen in figure 2 the ultimate tensile strength and the yield strength scale with external sample size in a power law fashion. This phenomenon is generally referred to as "smaller is stronger". The increase of the strength of nano pillars with decreasing diameter is an example of an *extrinsic* classical size effect. The word classical here indicates that this is not a quantum mechanical phenomenon, and can be understood with classical physics theory. Now the material no longer can be described by its intrinsic microstructure and corresponding length scales, but also the extrinsic dimensions play a non-trivial role in the determining the final bulk material properties.

Many materials found in nature exhibit structure on more than one length scale. This structural hierarchy can play a major part in determining the bulk material properties. Take for example the wings of a butterfly (see also figure 3). These wings are made out of polysaccharide chitin. However the optical properties cannot be explained with knowledge of polysaccharide chitin and its specific microstructure. Instead the optical properties are mostly determined by the *hierarchy* or gyroid structure of the material at a larger scale. Just like a periodic electrostatic potential causes a material to be a semi-conductor, so does a periodic dielectric constant gives rise to a photonic band gap. This is an example of an photonic crystal and the photonic properties are determined by the *architecture* of the material.

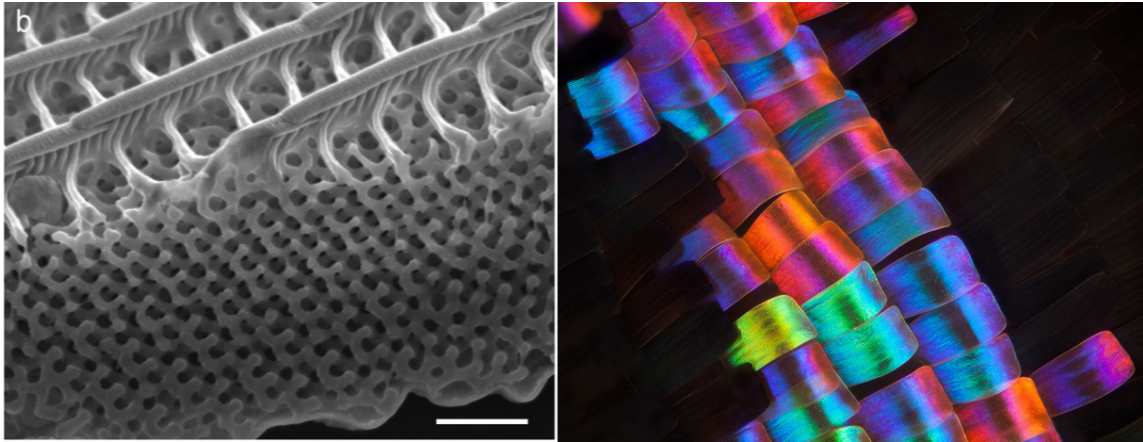


Figure 3: Left figure: Scanning electron microscope image of a butterfly wing (*Callophrys rubi*). The scale bar indicates 1 μm . Right figure: Optical microscope image of a butterfly wing (*Callophrys rubi*). Taken from 4.

Using this concept of hierarchy is something which can be found in many different bio materials and engineering. Hard biomaterials found in nature such as mollusk shells, nacre and beaks obtain their resilience and damage tolerance, due to the hierarchical arrangements in their design 5 6 . Similarly within engineered structures, like the Eiffel Tower, the introduction of architectural elements provides a more efficient way to distribute the load-bearing capability when compared with the monolithic counterpart.

Due to advances in fabrication processes it is now possible to create *nanoarchitected structural metamaterials* which extends this concept of architecture to the micro- and nanometer length scales. These nanolattices are created using a three-dimensional (3D) polymer scaffold, which is made using two-photon lithography direct laser writing. Using a thin film deposition technique a thin film of material is then deposited onto the polymer scaffold, such that it coats the entire surface. By removing part of the coated structure by focused ion beam milling (FIB) and putting the entire sample in O_2 plasma the internal polymer is etched away. The result is a 3D freestanding nanolattice consisting of a network of hollow tubes, as shown in 4. At these reduced dimensions extrinsic classical size effects can decouple coupled material properties, which creates the possibility to make metamaterials with amplified properties. It has been shown that using a hollow-tube alumina nanolattice with an octet-truss geometry created a strong, stiff and simultaneously lightweight material 7 .

The power of *nanoarchitected structural metamaterials* is that the hierarchy of length scales that characterizes nanotrusses spans several orders of magnitude-unit cell widths are several microns, truss member diameters are hundreds of nanometers, and wall thicknesses are tens of nanometers 8 . In this way it is possible to use size effects, which manifest themselves at the nanoscale, to change the material properties at micro, meso and macro scale. Hierarchical materials can thus outperform bulk materials because the length scales governing various physical processes are decoupled 9 . Additionally the large control of the exact architecture gives control over the final material properties, shifting the material science paradigm from *structure* \rightarrow *processing* \rightarrow *properties* to *property* \rightarrow *architecture* \rightarrow *fabrication*.

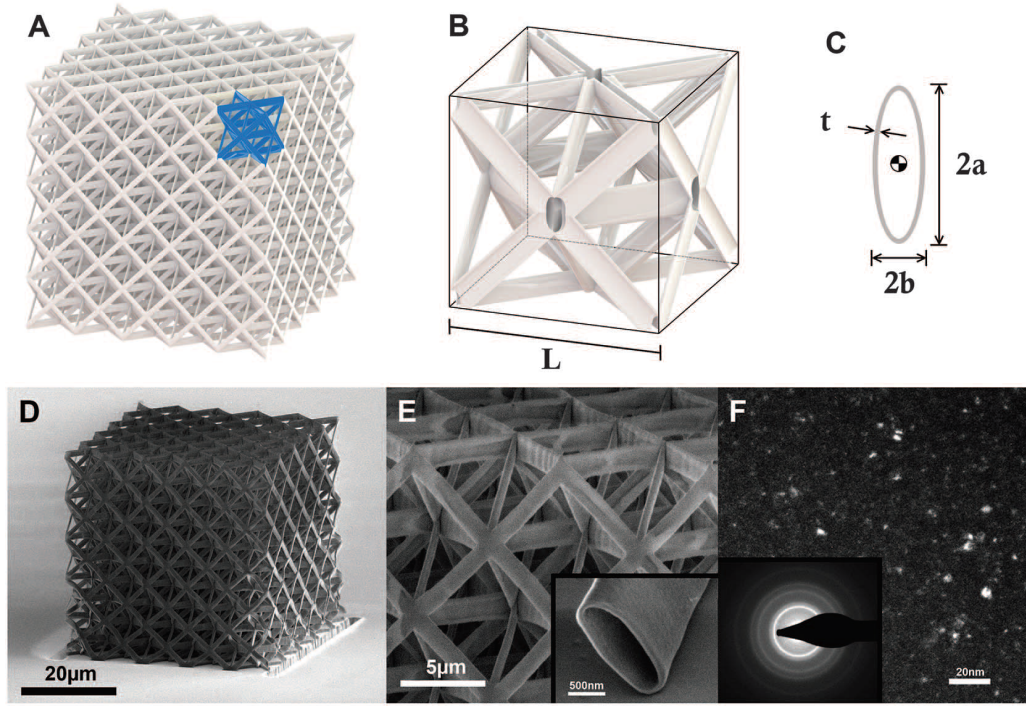


Figure 4: Architecture, design, and microstructure of alumina nanolattices. (A) CAD image of the octet-truss design used in the study. The blue section represents a single unit cell. (B) Cutaway of hollow octet-truss unit cell. (C) Hollow elliptical cross section of a nanolattice tube. (D) SEM image of alumina octet-truss nanolattice. (E) Zoomed-in section of the alumina octet-truss nanolattice. The inset shows an isolated hollow tube. (F) TEM dark-field image with diffraction grating of the alumina nanolattice tube wall. Taken from 7 .

Specifically for applications where combinations of properties in multiple physical domains are required using nanoarchitected materials could prove beneficial. Just like there is a coupling between the weight and the strength of a material, there are no materials which have ultra low density and thermal conductivity and yet high stiffness. For example, the hardest known material, diamond, also has the highest thermal conductivity 10 . Conversely, materials with ultralow thermal conductivity, such as graphene foams, polymer foams, carbon nanotube (CNT) films, CNT sponges, CNT aerogels, and silica aerogels, have poor mechanical properties. A material that combines the desired properties in both the mechanical and thermal domains remains unrealized 8 . These type of materials could be used as the thermal protection system of a spacecraft, since for these type of systems one requires lightweight materials that can withstand large mechanical stresses and thermal gradients.

The objective of this thesis is to designing, fabricate and characterize nanoarchitected materials with simultaneously low density and thermal conductivity and yet high stiffness. The thesis starts off with an overview of the relevant theory. After the general theoretical background and objective has been set out in the previous section the fundamentals of the 3w method (method to determine thermal conductivity), the mechanical experiments and device fabrication will be discussed. Finally the thesis will conclude with the experimental results, discussion and conclusions.

II. THEORY

We start off with a review of the relevant theory. Specifically the theoretical background of the mechanical and thermal properties of nanolattices will be discussed. Details of the fabrication process of these materials will be postponed to a later section. The theoretical section will start off with a discussion the mechanical properties of architected nano materials. After that the most relevant literature on classical thermal size effects are reviewed and the formal two dimensional analytical model of the heat transport is introduced. The theory section ends with the procedure of how the thermal conductivity is obtained from the data together with the associated statistics.

I. Mechanical properties of nanolattices

As described in the introduction section nanolattices can have improved mechanical properties with respect to their bulk counterpart due to a better load redistribution or the presence of extrinsic size effects. Within this research the following materials are used to make nanolattices: IPS (polymer photo resin), alumina and amorphous silicon. No mechanical size effects are expected, so an in depth discussion on this topic is omitted and can be found in 11 .

Instead next to size effects also another phenomenon related to the architecture of the material can be found in nano architected materials. The nanolattice depicted in figure 4 has an octet unit cells, which consists of hollow alumina tubes. What has been shown that for specific architectures that these nanolattices exhibited nearly full recoverability after compressions in excess of 50 % strain. Specifically it was shown that the ratio of the wall thickness and ratio of the beams comprising the octet unit cell is smaller than a certain fraction nanolattices become recoverable.

An example of this is shown in figure 5 . Here the snapshots of a compression of two different samples are shown, one nanotruss with a high solid fraction and one nanotruss with a low solid fraction. The sample with a high solid fraction fails in a catastrophic manner when strained more than a certain percentage. This can be expected because the nanotruss is entirely made out of alumina which is a brittle ceramic.

However when the wall thickness is reduced from 50 nm to 10 nm the nanolattice almost completely recovers after being strained more than 50 %. Samples with thin walls first deform elastically, where stress increased linearly with strain, followed by a ductile-like, controlled deformation, with stress plateauing after yielding.

This phenomenon in hollow ceramic nanolattices can be understood by understanding the failure mechanism in hollow tubes. When the local stress within these tubes surpass the yield stress the tube starts to plastically deform and due to the brittle nature of the ceramic eventually catastrophically fail in a brittle manner. However next to yielding the constituent beams can also buckle (both shell and beam). Dependent on the wall thickness, the beam radius and the material properties the stress at which this buckling occurs can be calculated. When this stress is below the yield stress the material will buckle instead of yield, resulting in a recoverable behavior.

Setting the stress necessary to onset yield and local shell buckling equal to each other we can obtain the ratio for the wall thickness t and the beam radius r for which the transition from catastrophic failure to recoverable behavior is expected. Similar expression can be obtained for

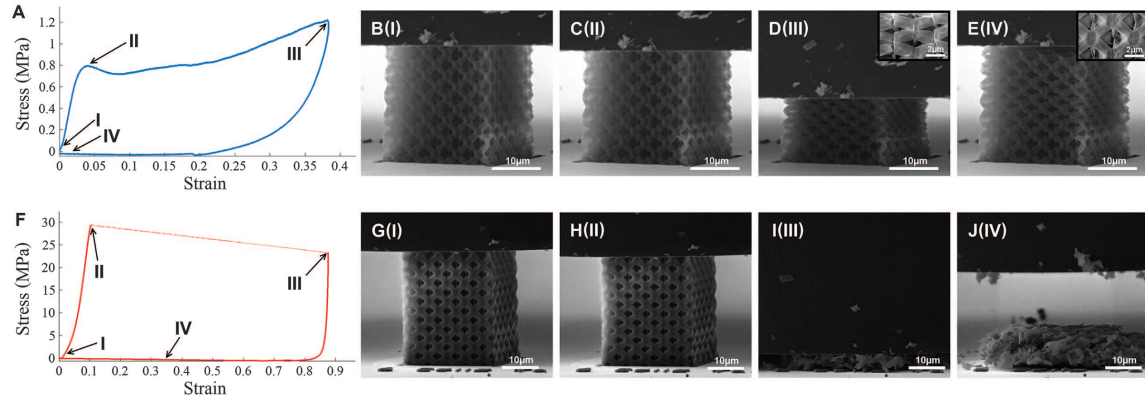


Figure 5: Compression experiments on thick- and thin-walled nanolattices. (A to E) Mechanical data and still frames from the compression test on a thin-walled ($L = 5$ mm, $a = 650$ nm, $t = 10$ nm) nanolattice demonstrating the slow, ductile-like deformation, local shell buckling, and recovery of the structure after compression. (F to J) Mechanical data and still frames from the compression test on a thick-walled ($L = 5$ mm, $a = 790$ nm, $t = 50$ nm) nanolattice showing catastrophic brittle failure and no post-compression recovery. Taken from 7 .

Euler beam buckling as a function of the beam radius r and the length of the beams L . Equating both relations the following expression for the transition between fracture and elastic failure are observed (see for full derivation reference 7) at the following critical ratio's

$$\left(\frac{t}{r}\right)_{\text{crit}} = \frac{\sigma_{\text{fs}}}{E} \sqrt{3(1 - \nu^2)}$$

$$\left(\frac{r}{L}\right)_{\text{crit}} = \frac{3}{\pi} \sqrt{\frac{2\sigma_{\text{fs}}}{5E}},$$

where σ_{fs} is the fracture strength of the material, ν is the materials poisons ratio and E is the materials youngs modulus. For hollow alumina beams the ratio of the thickness of the wall t and the radius of the elliptical beams r equals $(t/r)_{\text{crit}} \approx 0.02$.

II. Thermal properties of nanolattices

As described in the introduction the nano architected materials studied in this research will consist of a network of hollow tubes as is shown in figure 4 . The thermal properties of such structures are determined by several factors. The first factor influencing the thermal properties is off course the thermal properties out of which the material is made. Secondly there is an dependence on the specific architecture and its corresponding solid fraction. Lastly the potential presence of size effect could further impact the thermal properties. All three factor will be discussed in this section and we will start with discussing how size effects can emerge in nano architected materials.

Thermal classical size effects in thin films

To understand why classical size effects may occur it is import to note that nanolattices are made out of hollow tubes. It can be viewed as a two dimensional film wrapped around a three dimensional architecture. Within non-metallic crystalline materials the major carrier of heat are the phonons within the material. It has been a well established phenomenon that within thin films the thermal conductivity of these type of materials is reduced when the thickness of the film is less than the length scale of their phonon mean free path. 27 To understand this consider

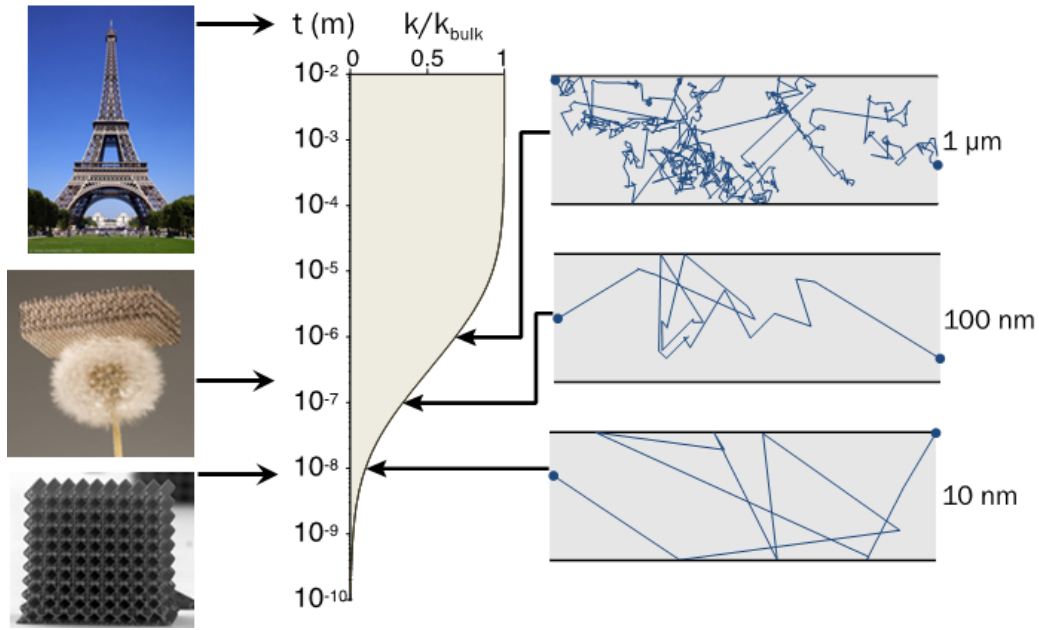


Figure 6: Schematic indicating the principle of thermal size effects in thin films. Left figures (from top to bottom): Eiffel tower of Paris, micro lattice and nano lattice. Middle figure: Thermal conductivity normalized by the bulk thermal conductivity as a function of film thickness. Right figures: schematic of phonon scattering events for different film thicknesses.

figure 6 . When the film thickness is large compared with the phonon mean free path (PMFP) no reduction of the thermal conductivity with respect to the bulk is observed, because the phonons tend to scatter much more frequently within the bulk than with the surface. However when the film thickness is comparable with the PMFP, the thermal conductivity is reduced due to incoherent boundary scattering of phonons ballistically traversing the film. This motivates the need for nanolattices instead of microlattices or other macroscopic architectures, because it is at these reduced dimensions these size effects are more profound.

Within amorphous materials similar effects can occur, but the description and physics is slightly different. Amorphous materials lack atomic periodicity so it is not possible to define a spectrum of phonons. Instead the vibrational modes are classified into delocalized (phononlike) modes called "propagons"; nonpropagating, delocalized modes called "diffusons"; and nonpropagating, localized modes called "locons".²⁷ It has been shown in previous research that for amorphous silicon the propagons can contribute significantly to the thermal conductivity.¹³

The thermal conductivity of thin film amorphous silicon as a function of film thickness is shown in figure 7 . What can be seen here is that the thermal conductivity as a function of film thickness is relatively flat up to approximately 100 nm. This is because the contribution of the propagons to the thermal conductivity is so much suppressed that the diffusons contribute much more to the thermal conductivity. When the film thicknesses becomes greater than 100 nm propagons start to contribute substantially to the thermal conductivity increases, which increases from 1 W/mK to the bulk thermal conductivity value of 4 W/mK. Due to the mean free path distribution of the propagons no size effects are expected in alumina.²⁷

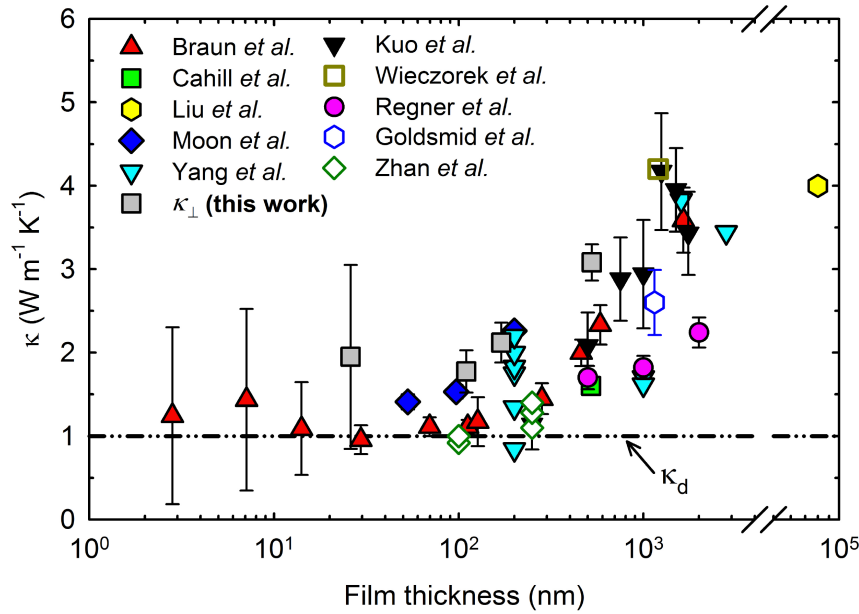


Figure 7: The experimental determined thermal conductivity of thin film amorphous silicon as a function of film thickness. Taken from 13 .

Numeric modeling of heat transport in nanolattices

Next to size effects also the architecture of the device influences the thermal properties. This is due to the fact that the geometry determines the effective distance the geometry needs to travel. In the absence of size effects the thermal properties of nanolattices can simply be modeled using a finite element program like COMSOL. In the left part of figure 8 a schematic representation is given of the modeled geometry. This geometry represents two octet unit cells with solid beams with a unit cell width of $25 \mu\text{m}$ stacked on top of each other together with a solid plate on top.

The thermal conductivity is determined by prescribing a fixed heat flux Q on the top and a fixed temperature on the bottom. From Fourier's law the thermal conductivity, k_{thermal} , is then given by

$$k_{\text{thermal}} = -\frac{Q}{\Delta T},$$

where ΔT is the temperature difference between the top and bottom. The finite element results for this geometry, taking the bulk thermal conductivity properties of PMMA, are depicted in the right hand side of figure 8 .

In the case size effects are present using finite element simulations is not appropriate because the simulations assume bulk values for the thermal conductivity of the used material. Therefore to incorporate the size effects which could be present in hierarchical materials another simulation approach is needed. The paper written by Dou et al. 8 solved the the spectral Boltzmann transport equation with the relaxation time approximation for an single crystalline silicon hierarchical material with octet unit cell (see also figure of 9). What they showed is that within single crystalline nannolattices the thermal conductivity can be reduced by an order of magnitude when compared

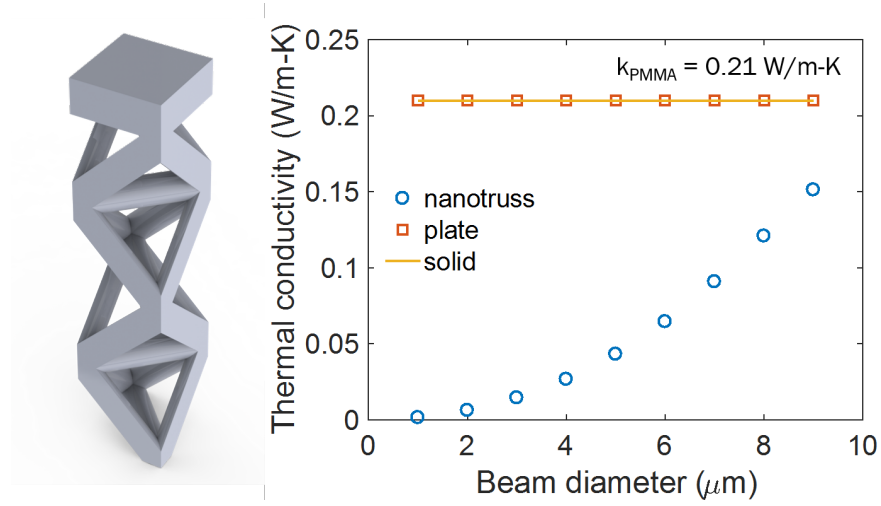


Figure 8: Left figure: schematic representation of geometry which is modeled. Right figure: Thermal conductivity as a function of the beam diameter of the octet unit cell with unit cell width of 25 μm assuming a bulk thermal conductivity of PMMA. Simulations courtesy of Nicholas Dou.

with the finite element simulations. As is expected the wall thickness is the key variable dictating the size effect and the other architectural features influence the finite element and BTE results in a similar manner.

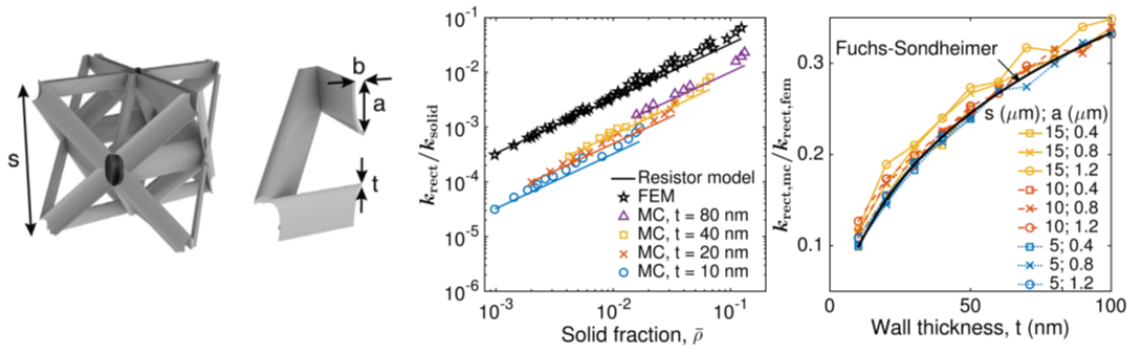


Figure 9: First and second figure: schematic representation of geometry which is modeled. Third figure: The thermal conductivity normalized by the bulk thermal conductivity of single crystalline silicon nanolattices for different wall thicknesses as a function of solid fraction. Fourth figure: Third figure: The thermal conductivity normalized by the finite element results for different geometries as a function of wall thickness. Taken from 8 .

Analytical solutions of of heat transport in nanolattices

Within this research the thermal properties of the nanolattices will be determined using an experimental technique used extensively to determine the thermal properties of thin films. Within this section the formal 2D analytical model of the heat transport within nanoarchitected materials

is going to be introduced. To obtain an analytical solution an approximation is made, which is depicted in figure 10 . Within the experiment a gold heater will periodically heat the top of the experimental hierarchical structure, which is situated on top of a silicon chip. It is assumed that the heat transport through the nanolattice is one dimensional, which boils down to treating it as a homogeneous material with an effective thermal conductivity.

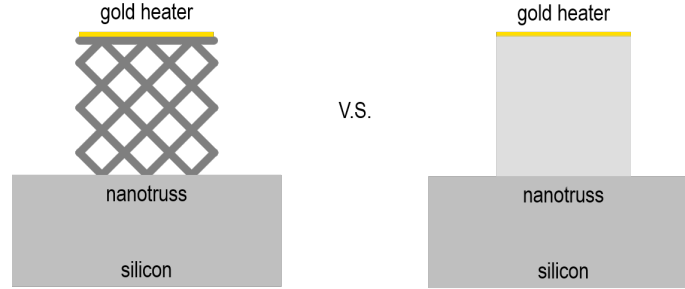


Figure 10: Left figure: Schematic representation of the device geometry used in the experimental setup. Right figure: Simplification of the device geometry used to obtain an analytical expression for the temperature profile at the heater line.

The two-dimensional heat-conduction model of the remaining layered structure has been solved by T. Borca-Tasciuc et al. ¹⁵ The integral Fourier transformation technique is used to obtain an analytical solution for a periodic heating of the gold heater line and a prescribed boundary condition (adiabatic/isothermal/semi-infinite). ¹⁶ Neglecting the contributions from the thermal mass of the heater and thermal boundary resistances between different layers the complex temperature rise of a heater dissipating a periodic $\frac{p_{2\omega}}{l}$ [W/m] electrical power, with peak power p , per unit length is given by

$$\Delta T_{2\omega} = \frac{-p}{\pi l k_{y1}} \int_0^\infty \frac{1}{A_1 B_1} \frac{\sin^2(b\lambda)}{b^2 \lambda^2} d\lambda,$$

where

$$A_{i-1} = \frac{A_i \frac{k_{yi} B_i}{k_{yi-1} B_{i-1}} - \tanh(\phi_{i-1})}{1 - A_i \frac{k_{yi} B_i}{k_{yi-1} B_{i-1}} \tanh(\phi_{i-1})}, \quad i = 2, \dots, n$$

$$B_i = \left(k_{xyi} \lambda^2 + \frac{i2\omega}{\alpha_{yi}} \right)^{1/2},$$

$$\phi_i = B_i d_i, \quad k_{xy} = k_x / k_y,$$

where, n is the total number of layers including the substrate, subscript i corresponds to the i th layer starting from the top, subscript y corresponds to the direction perpendicular to the film/substrate interface, b is the heater half width, k is the thermal conductivity of the layer, ω is the angular modulation frequency of the electrical current, d is the layer thickness, and α is the thermal diffusivity. In this case the number of layers n is three, $n = 3$. The layers are a top plate, the nanolattice and the silicon substrate. The 1D assumption is implemented by taking k_x to be

zero for both the top plate and the nanolattice. The boundary condition is determined by the value of A_n , here the frequency range will be chosen such that the results are independent of the boundary conditions at the bottom of the silicon substrate.

III. Determining the thermal conductivity of nanolattices

The exact way how the temperature of the heaterline is determined will be discussed in the next section. Here we will present the estimation procedure how, given the data, the thermal conductivity values are obtained. For different driving frequencies ω the complex temperature of the heater line, $T(\omega)_{\text{data}}$ can be measured. Then for a specific set of variables, $v = [v_1, \dots, v_n]$ containing all the information of each layer, this can be compared with the complex temperature predicted by the model $T(\omega, k)_{\text{model}}$. Here $v_i = [k_{x_i} \ k_{y_i} \ \alpha_i \ d_i]$ contains all the variables of layer i which are used in the analytical model. Now define the following objective function SSR,

$$\text{SSR} = \sum_{i=1}^N |T(\omega_i)_{\text{data}} - T(\omega_i, v)_{\text{model}}|^2. \quad (1)$$

Lastly let the specific set of variables be separated into variables we can measure (v_M) and variables we would like to fit (v_F), i.e. $v = [v_M + v_F]$. Then using non linear least squares the non linear least squares estimator of v_F , \hat{v}_F , can be obtained by minimizing the sum of squared residuals. More specifically using a Levenberg-Marquardt algorithm \hat{v}_F is the argument which minimizes the objective function SSR, i.e.

$$\hat{v}_F = \underset{v_F}{\text{argmin}} \text{SSR}(v_F). \quad (2)$$

Now let the jacobian, J , be defined as the matrix with all first-order partial derivatives of the vector valued function $T(\omega_i, v)_{\text{model}}$. The i^{th} row and the j^{th} column of J , J_{ij} are then given by

$$J_{ij} = \frac{\partial T(\omega_i, v)_{\text{model}}}{\partial v_{Fj}}$$

The variance-covariance matrix of the estimator \hat{v}_F is then given by

$$\text{VAR}(\hat{v}_F) = \frac{\text{SSR}(\hat{v}_F)}{N - k} (J^T J)^{-1},$$

where k is the number of elements in \hat{v}_F .

The standard error of the elements in \hat{v}_F are then easily computed by taking the square root of the diagonal terms of the variance matrix. The only problem with this procedure is that it only takes into account the statistical errors and not the systematical errors. Within the following relation

$$T(\omega_i)_{\text{data}} = T(\omega_i, v)_{\text{model}} + \epsilon_i,$$

it is assumed that the entire uncertainty is contained within ϵ_i and that the measured variables within v , v_M , are known exactly. However in reality this is off course measured with a certain uncertainty and neglecting could potentially underestimate the error bounds.

The way this inconsistency is resolved, is by making use of a procedure called bootstrapping.

Instead of taking v_M to be a fixed variable it is assumed that every element of $v_M = [v_{M_1}, \dots, v_{M_N}]$ follows a specific distribution, i.e.

$$\begin{aligned} v_{M_1} &\sim f_1(\Theta_1), \\ &\vdots \\ v_{M_N} &\sim f_N(\Theta_N), \end{aligned}$$

where Θ_i contain the parameters of the distribution. The parameters and the distribution are chosen such that the average is equal to the measured value and the standard deviation reflects the uncertainty.

Now the bootstrapping procedure starts with taking a random draw from these distributions and to define a new objective function SSR as defined in equation 1. Using this objective function a new estimate for $\hat{\nu}_F$ can be obtained from equation 2. The result is stored and this sampling is done a sufficient amount of times until the posterior distribution of $\hat{\nu}_F$ has converged. Now a 95 % confidence interval can be obtained by sorting the results and take the $\frac{0.025}{N}$ th and the $\frac{0.975}{N}$ th sorted estimate.

The 95% confidence interval is a measure of the uncertainty in the estimated parameter. Due to the low pass filter in the 3ω setup the signal is measured with little noise. Due to this low noise levels the statistical error as calculated by the fitting procedure becomes unrealistically small. This is because this error does not take into account the systematic errors. By using the bootstrapping procedure these systematic errors can be dealt with by specifying the distributions of all the parameters used in the model, which eventually will lead to the confidence intervals.

IV. Mechanical properties of nanolattices

Next to the thermal properties also the mechanical properties of nanolattices will be determined. Specifically the stiffness will be determined using uniaxial compression experiments. In this research only unit cells with octet geometry are used. An nanolattice with a unit cell which has an octet geometry with solid beams is an example of a stretching dominated structure. The strength and deformation of an ideal, monolithic, stretching-dominated cellular solid is governed by stretching of the beams, with the nodes acting as rigid pin-jointed elements that perfectly transfer load between truss members. For stretching dominated structure the stiffness, E , and the yield strength, σ_y should scale linearly with (relative) density 19 ,

$$\begin{aligned} \sigma_y &\propto \rho, \\ E &\propto \rho. \end{aligned}$$

However in our case the octet unit cells are comprised of hollow beams. Now, the nodes are constrained only by the shell walls, which has a detrimental effect on strength and stiffness because load transfer at the nodes occurs via shell wall bending. This, together with the sharp angles between the tubes, leads to an uneven distribution of stress and induces large stress concentrations in the vicinity of the nodes. 11

As described in the introduction the properties of nanolattices can be controlled by their architecture. For unit cells with hollow octet geometry the most important parameters in the

parameters space are the ratio's $\frac{r}{L}$ and $\frac{t}{r}$. To see how these ratio's influence the mechanical properties consider figure 11. Here the simulated stiffness (using finite elements) is depicted for different radii. What can be seen here is that in the low density region there is a linear relation between stiffness and density. However at larger densities it can be seen that the simulated stiffness actually decreases with relative density due to weakening of the nodes with increasing radius.

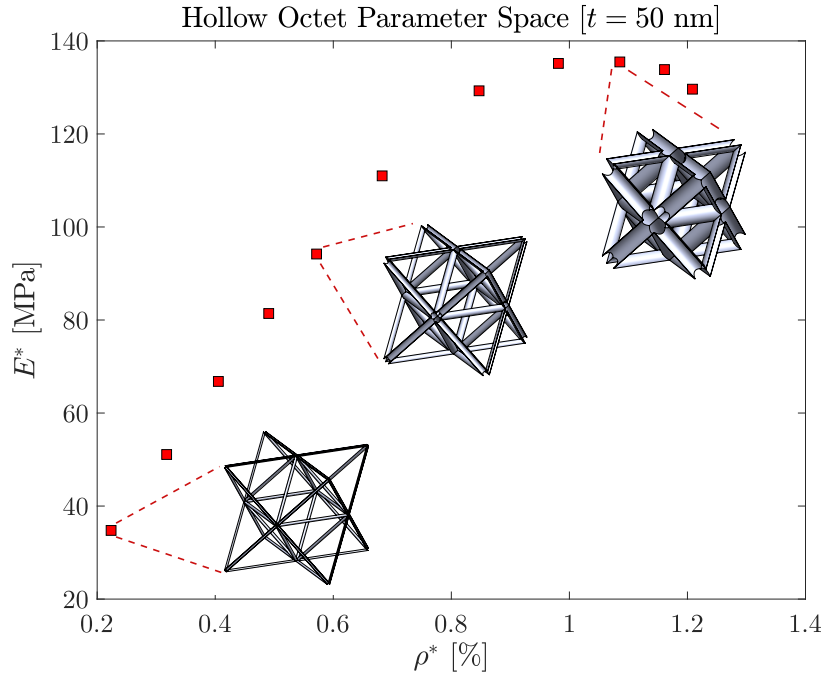


Figure 11: The simulated stiffness of a hollow octet alumina nanolattice for varying radius with wall thickness equal to 50 nm and unit cell width of 25 μm . The stiffness are calculated for $r = 0.25, 0.375, 0.5, 0.625, 0.75, 0.9375, 1.25, 1.5625, 1.875, 2.1875, 2.5$. Simulations courtesy of Carlos Portela.

III. EXPERIMENTAL SETUP

Now that the theoretical background and objectives have been set out in the previous sections it is time to introduce the experiment setup. We will start of with explaining how the thermal properties will be determined. After this also the experimental setup used to measure the mechanical response of the nanolattices will be discussed.

I. Temperature measurement

As was depicted in figure 10 in order to heat up the nanolattice on the top and measure the temperature on the top a gold heater line will be deposited on top of the sample. In this section it will be explained how exactly the temperature is determined using a 4 point probe. Consider the top left figure in figure 12 . Here a thin film is deposited on top of a substrate, with a gold heater

line on top together with four gold pads.

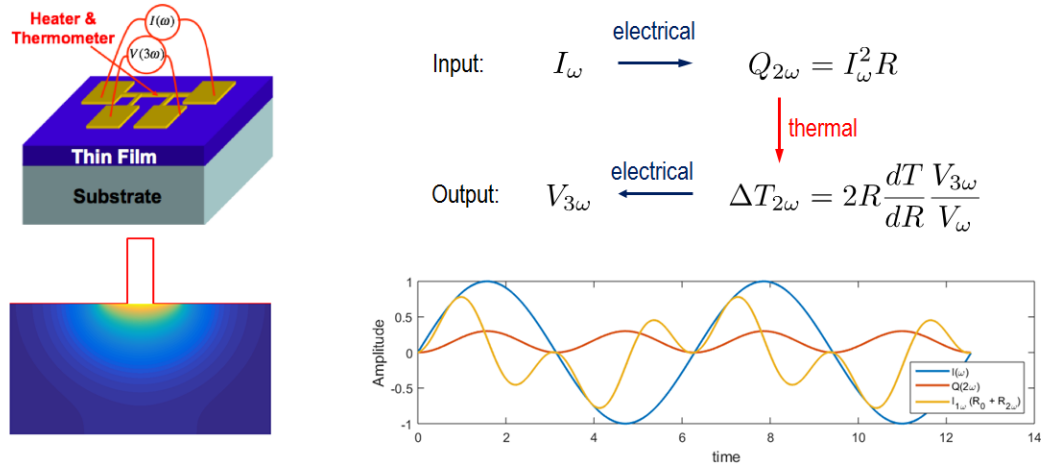


Figure 12: Top Left figure: Example of a 4 point probe on top of a thin film. Top Right figure: Flow diagram relating the input current and measured voltage to the input heating and resulting temperature. Bottom left: Example of the heating profile created inside the substrate. Bottom right: Example signals of the current (blue), heat flow (orange) and resulting voltage (yellow) as a function of time.

Through 2 of the 4 pads a periodic current will flow with frequency ω as indicated. Because of this the thin line between the two pads will start to heat up. This heating will oscillate at a frequency of 2ω because the heating $Q_{2\omega}$ is given by

$$Q_{2\omega} = I_{\omega}^2 R,$$

which is indicated in orange in the top right figure of figure 12 . This oscillating heat flow will cause the temperature of the heater line to also start oscillating with a frequency of 2ω with a certain phase lag ϕ . The change in temperature cause the resistivity of the heater line to change. Therefore also the resistance of the heater line will have a small oscillation at a frequency of 2ω . Doing a first order Taylor expansion the resistance of the heater line is given by

$$R = R_0 + \left(\frac{dR}{dT} \right) \Delta T_{2\omega} \cos(2\omega t + \phi)$$

Because the resistance oscillates this also perturbs the voltage signal, V , measured across the other two pads. Using the relation for the resistance of the heater line this voltage can be written as

$$\begin{aligned} V &= I_{\omega} \sin(\omega t) R \\ &= R_0 I_{\omega} \sin(\omega t) + I_{\omega} \left(\frac{dR}{dT} \right) \Delta T_{2\omega} \cos(2\omega t + \phi) \sin(\omega t) \\ &= V_0 \sin(\omega t) + \frac{V_0}{R_0} \left(\frac{dR}{dT} \right) \frac{\Delta T_{2\omega}}{2} [\sin(3\omega t + \phi) - \sin(\omega t - \phi)] \\ &= \left(V_0 \sin(\omega t) - \frac{1}{2} \frac{V_0}{R_0} \left(\frac{dR}{dT} \right) \Delta T_{2\omega} \sin(\omega t - \phi) \right) + \left(\frac{1}{2} \frac{V_0}{R_0} \left(\frac{dR}{dT} \right) \Delta T_{2\omega} \sin(3\omega t + \phi) \right) \\ &= V_{1\omega} \sin(\omega t + \chi) + V_{3\omega} \sin(3\omega t + \phi) \\ &\approx V_{1\omega} \sin(\omega t) + V_{3\omega} \sin(3\omega t + \phi), \end{aligned}$$

where in the last step it was assumed that the temperature variation is too small to change the phase of the voltage at ω .

Using these relations the temperature fluctuations at a frequency of 2ω can be rewritten in terms of the measured voltages,

$$\Delta T_{2\omega} = 2 \frac{dT}{dR} R \frac{V_{3\omega}}{V_{1\omega}}$$

So by measuring the voltage across the heater line and determining the component of the voltage which oscillate at 1ω and 3ω one can use the above relations to determine the heating and temperature profile. Then using the measured temperature and applied heating the transfer function coupling the two, $H_{2\omega}$, in the following relation

$$\Delta T_{2\omega} = H_{2\omega} Q_{2\omega}, \quad (3)$$

can be determined. As is explained in the previous section knowledge of this transfer function can be used to determine the thermal properties.

II. 3ω experiment.

As explained in the previous section the temperature profile of the heater line can be determined by measuring the voltage at 1ω and at 3ω , therefore this experiment is generally referred to the three omega experiment. Within this section the exact experimental setup of the 3ω is described.

An schematic representation of the measurement sample is depicted in the top of figure 13 . Instead of having a gold heater line on top of a thin film there will be a nanolattice between the gold heater line and the substrate. The cross section of the device architecture resembles the 2D schematic which is used in the 2D thermal model. The exact fabrication process will be discussed at a later stage.

The experimental setup is depicted in the bottom figure of figure 13 . The setup consists of a current source, resistor box, samples, electronic amplifiers and control and measurement devices. The current supplies a fixed alternating current at a frequency of ω which is send through a resistor box and a sample. The voltage across the sample and resistor box are measured using a lock-in amplifier and subsequently read out by the computer.

The reason why the resistor box is placed in between is to cancel any unwanted 3ω signal which could come from the current source or any other external electronic noise. The way this cancellation is done is by measuring the voltage of both the resistor box and the sample. Then both signals are subtracted by the lock-in amplifier. Since the resistor box is an macroscopic resistor the temperature rise can be neglected and hence no three omega voltage will be induced by the current flowing through it. Any unwanted 3 omega voltage created in the circuit will cause a 3ω current in the resistor box and in the sample. When the resistance of the heater line and the resistor box are the same this will lead to an equal voltage drop. This equality in voltage is guaranteed by placing a digital to analogue converter between the buffer and the lock-in. Hence subtracting the 3ω voltage measured across the resistor box from the 3ω voltage measured across the sample will cancel any unwanted (external) contributions and what you are left with is the three omega voltage you are interested in.

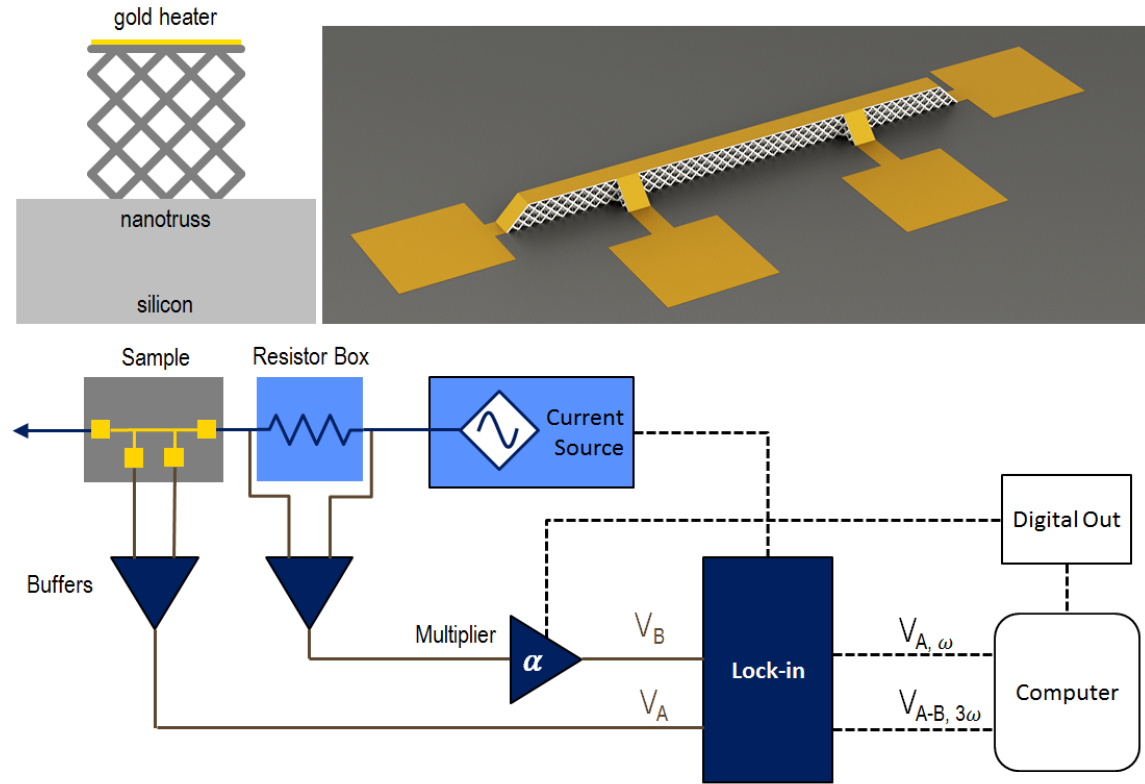


Figure 13: Top figures: Schematic representation of the cross section which will be used in the modeling (left figure) and the CAD drawing of the device geometry used in the experimental setup (right figure). Bottom figure: Schematic representation of the electronics used in the 3ω experimental setup.

Between the lock-in amplifier and the sample and resistor box buffer amplifiers are placed. These buffer amplifiers simply copy the signal and are placed in between to make sure that the measurement electronics do not interfere with the signal you are interested in. The voltages are then measured by a lock-in amplifier, which is able to detect and measure very small AC signals. Lock-in amplifiers use a technique known as phase-sensitive detection to single out the component of the signal at a specific reference frequency and phase. The lock-in receives a triggering signal from the current source, which gives information about the frequency and the phase. Using this triggering the lock-in amplifier creates its own reference signal, V_{ref} . The output of the phase sensitive detector, V_{PSD} , is then simply the product of the input signal, V_{sig} , and its own reference signal, i.e.

$$\begin{aligned} V_{PSD} &= V_s V_r \sin(\omega_s t + \theta_s) \sin(\omega_r t + \theta_r) \\ &= \frac{1}{2} V_s V_r \cos([\omega_s - \omega_t]t + \theta_s - \theta_r) - \frac{1}{2} V_s V_r \cos([\omega_s + \omega_t]t + \theta_s + \theta_r), \end{aligned}$$

where ω indicates the frequency, θ indicates the phase, V indicates the signal amplitude and the subscript s and r indicate the signal and reference signals. When this signal is then passed through a low pass filter such that all the AC signals are removed, except for the part of the signal which

has the same frequency as the reference signal. Now V_{PSD} becomes

$$V_{\text{PSD}} = \frac{1}{2} V_s V_r \cos(\theta_s - \theta_r),$$

which gives information on both the amplitude as well as the phase of the signal. Specific details on which settings to use on the lock-in amplifier can be found in reference 17 .

III. Mechanical compression experiments

Next to determining the thermal properties of nanolattices also the mechanical properties of nanolattices will be measured. Specifically using uniaxial compression tests the stiffness will be determined. Within the simulations periodic boundary conditions were assumed, which is similar to assuming that the nanotrusses extends infinitely in the lateral dimensions. However due to limitation in writing speed finite samples have been made. For the compression experiments separate samples have been fabricated comprising 5 by 5 by 5 octet unit cells. Details on the fabrication method will be discussed in the next section. The uniaxial compression experiments were performed on nanolattices in a G200 XP Nanoindenter (Agilent Technologies). The test structures were compressed uniaxially to a strain of $\sim 40\%$ at a strain rate of 10^{-3}s^{-1} . At these strain rates the compression can be considered quasi static. To observe the deformation mechanism some compression test have also been preformed in-situ in the SEM using an InSEM Microprobe system.

IV. SAMPLE FABRICATION

Now that the experimental setup is described in detail it is time to discuss the fabrication of the device shown in figure 13 . This section will start off with explaining how to write arbitrary complex patterns in three dimensions using two photon lithography. Secondly the thin film deposition techniques used in this research, atomic layer deposition and plasma enhanced chemical vapor deposition, will be introduced. Finally the remaining micro fabrication steps will be discussed. An schematic overview of the different fabrication steps have been depicted in figure 14 .

I. Writing structures using two photon lithography

Direct laser writing is a multiphoton lithography technique which enables you to write any arbitrary complex structure in three dimensional space. Within this section it will be explained how to write these structures out of a polymer.

In direct laser writing a photoresist is illuminated by laser light at a frequency below the single-photon polymerization threshold of the resist. However when the laser is focused to a focal point inside the photoresist the probability that two photons meet each other increases. One photon does not have enough energy to cross-link two monomers, however two photons do. Therefore when the intensity at the focal point is high enough it may exceed the threshold for initiating polymerization. That is the reason why direct laser writing is a multiphoton lithography technique. Now the resolution is no longer limited by the wavelength of the light used to write the structures, but by the size of the voxel created by the focal point of the laser. The structures are written using the Photonic Professional GT system, which uses a femto second pulsed laser with a wavelength

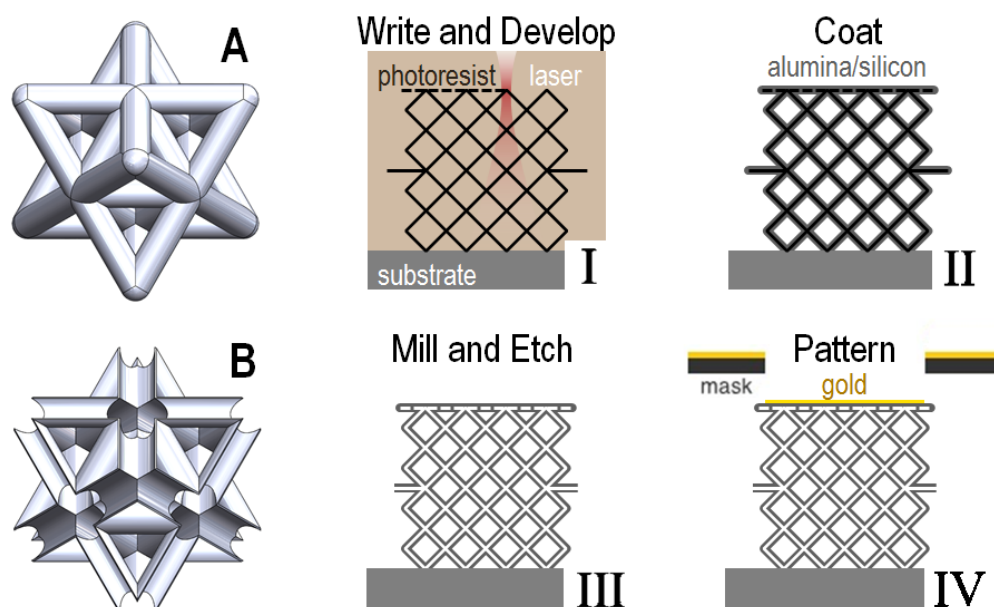


Figure 14: Left figures: CAD drawings of an octet unit cell with solid beams (A) and hollow beams (B). Center and right figures: fabrication steps used in creating the device consisting of octet unit cells with hollow beams. I: The programmed CAD drawing is written by locally cross linking the polymer in the photo resist and subsequently dissolving the non cross-linked polymer. II: The 3D structure is coated using atomic layer deposition or plasma enhanced chemical vapor deposition. III: The sacrificial beams are milled open using a focused ion beam and the entire structure is hollowed out by plasma etching. IV: Gold is deposited onto the structure using E-beam evaporation and a shadow mask.

of 780 nm. However it is able to write features with a 100 nm resolution. In the right part of figure 15 this process is illustrated using a similar phenomenon: two photon microscopy.

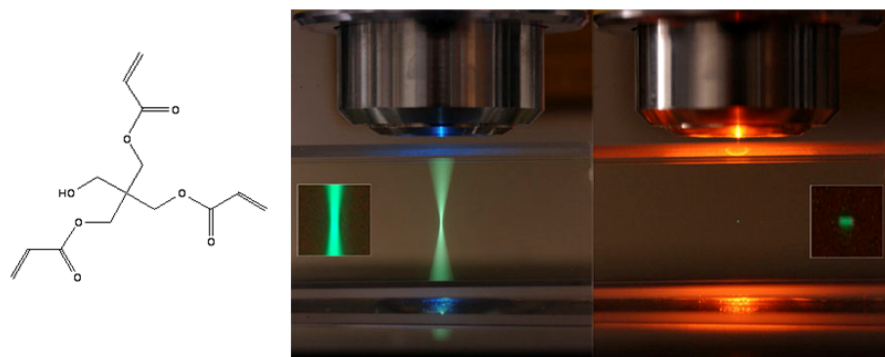


Figure 15: Left figure: Schematic representation of 2-(Hydroxymethyl)-2-[[1-(1-oxoallyl)oxy]methyl]-1,3-propanediyl diacrylate, the monomer present in IP-Dip. Right figure: regular microscopy (left) and two photon microscopy (right)

The photo resists used are commercially available negative photo resins under the name of IP-Dip

and IP-S. The monomer present in IP-Dip (weight content >95%) is depicted in the left part of figure 15 . When the laser pulse irradiates the photoresist it is absorbed by a photoinitiator present in the resin. This creates a radical cation which reacts with the unsaturated carbon bonds in the monomer. This can then react with another monomer creating elongated polymer chains. After the writing process the entire sample is submerged into propylene glycol monomethyl ether acetate, which dissolves the monomer. What you are left with is the complex three dimensional structure everywhere the voxel has cross-linked the monomer in the resin.

Any arbitrary geometry can be programmed. A convenient way is to achieve this is by making a CAD drawing in Solid Works. See also figure 14 A. This is then sliced into different layers where the layers are perpendicular to the z plane. These planes are then converted into a raster with a certain hatching distance. This is then converted into an STL file, which is a standard format for 3D printing.

II. Thin deposition techniques

Direct laser writing enables us to write any arbitrary pattern. The only problem is that this limits us to using organic materials. Therefore to access new materials classes the polymer scaffold is coated using a thin film deposition technique and the polymer is subsequently etched away using oxygen plasma, leaving a hollow shell like structure. Here two thin film deposition techniques will be used: atomic layer deposition and plasma enhanced chemical vapor deposition.

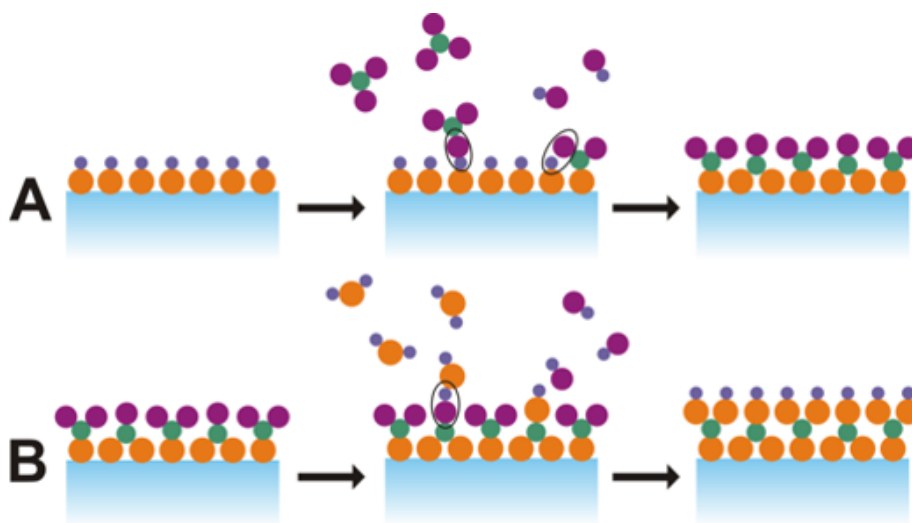


Figure 16: Schematic representation of the growth of one layer of alumina using atomic layer deposition. Colored spheres indicate the following atoms/molecules: Oxygen (orange), Hydrogen (blue), Purple (Methyl-group), Green (aluminum). Process A: Chamber is at vacuum conditions after which a pulse of precursor TMA (tri-methylaluminum) is let into the chamber. All the TMA dissociatively chemisorbs on the substrate surface leaving a surface covered with AlCH₃. Process B: Subsequently H₂O vapor is let into the chamber, which reacts with the surface methyl group forming methane as a reaction byproduct, which results in a Al₂O₃ surface.

Atomic layer deposition (ALD) is a conformal deposition technique which enables controlled film

growth with precision up to the angstrom level. An example of the ALD process for alumina is shown in figure 16 . The reaction is self limiting meaning that both processes A & B depicted in figure 16 are self limiting. The great advantages are that this method is a conformal coating technique and makes it possible to control the thickness on an atomistic scale. The big disadvantages is that the process is slow, with growth rates of 9 nm per hour.

Specifically conformity is a very useful property of the thin film technique, because it leads to the most structurally robust structures and it allows you to compare your experimental devices and measurements with the theoretical models. Alumina has advantageous properties for our research purposes, it combines high stiffness with low thermal conductivity. However it is not expected that there will be size effects present in alumina. In order to be able to observe size effects materials in which the phonons or propagons with large mean free path contribute significantly to the thermal conductivity. As has been discussed in the theory section amorphous silicon satisfies such criteria.

Unfortunately it is not possible to use ALD to deposit silicon. Another thin film deposition method is to use plasma enhanced chemical vapor deposition (PECVD). It can reach much faster growth rates, but the big disadvantages is that it is not a conformal coating technique. Just like with ALD of alumina the precursor silane (SiH_4) contains the atom of interest (Si) surrounded by organic atoms or molecules. As in ALD the silane precursor is adsorbed onto the surface. The difference with ALD is that the reaction is not self limiting and that dissociation of the precursor is caused by high energy electrons present in the plasma. So the film can grow continuously leading to growth rates on the order of 10 nm per minute. However this growth rate will be smaller far inside the structure than parts near the edge of the structure. Lastly the polymeric scaffold will degrade inside the plasma, therefore the structure needs to be protected by depositing one nm of alumina as a protection layer.

III. Hollowing out structures

After the polymer scaffold has been coated with either alumina or amorphous silicon the structure needs to be hollowed out and gold needs to be deposited on top of the structure. Here we will start off with explaining how the structures are hollowed out.

The polymer inside is etched away by placing the entire structure in oxygen plasma. In order to expose the polymer the outer structure needs to be opened up, because the oxygen plasma is not able to penetrate through the alumina or amorphous silicon. This is done by programming additional sacrificial beams into the structure, see also figure 14 III. Using a focused ion beam these beams are milled open such that the polymer is exposed. The entire structure is then placed into oxygen plasma until all the polymer is etched away.

To identify the total time needed to etch away the inside polymer, the structure is placed in oxygen plasma and intermittent SEM (scanning electron microscopy) pictures and EDS (energy dispersive spectroscopy) maps of the structure have been taken. See also figure 17 . In the figure the structure after 7 and 24 hours of etching are depicted. The structure is hollowed out from the bottom as can be seen by the moving etch front over time. Within 24 hours almost the entire structure has been etched out.

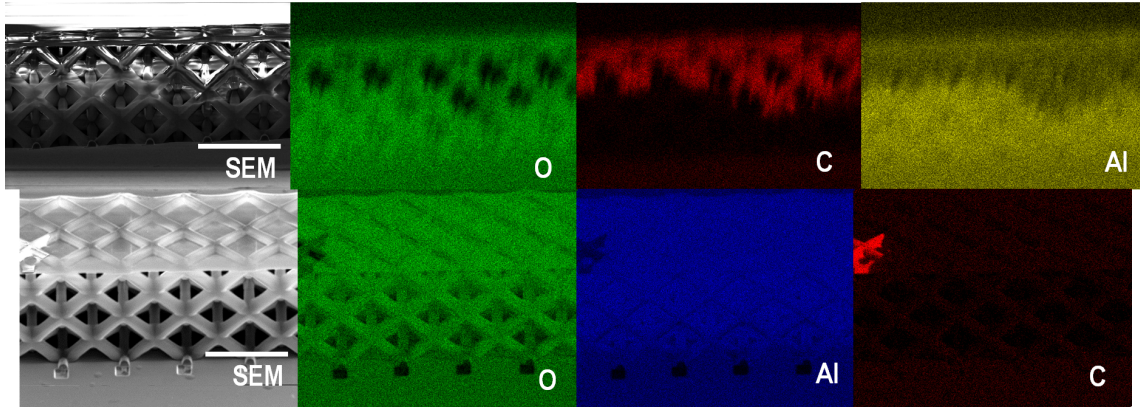


Figure 17: SEM figure and EDS map for oxygen(O) carbon(C) and aluminum (Al) of a the device after 7 hours of etching (top figures) and 24 hours of etching (bottom figures). The sacrificial beams are at the bottom of the structure.

The next step in the fabrication process is to deposit gold on top of the structure.

IV. Gold deposition onto structures

Now that the structure has been coated with either alumina or amorphous silicon and hollowed out subsequently it is time to deposit gold on top of the structure, as is depicted in figure 13 .

The most common route through which only parts of the substrate is covered with gold is by using a liftoff process. Not going into too much details a liftoff process is a photo lithography process in which a photo resist is spin coated onto a chip, heat treated and subsequently exposed to UV light. In our case a chrome mask has been used has been used to block the region where eventually the gold pattern should be. The photoresist used was a negative photoresist, which is a type of photoresist in which the portion of the photoresist that is exposed to light becomes insoluble to the photoresist developer. Putting the chip into the photoresist developer the unexposed region dissolves and the final result can be viewed in figure 18 .

In the trench of the pattern, where the gold will eventually go, the nanolattice can be written. The writing system can be programmed such that the pattern is aligned with the nanolattice. Then gold can be evaporated onto the structure and subsequently put into a bath of acetone for about 12 to 16 hours. The photoresist will dissolve in the acetone and it will lift-off the gold on top of it. This would result in the device architecture depicted in figure 13 .

The only problem is that in developing the nanolattice the entire chip is submerged into PGMEA to dissolve the not cross-linked polymer. The problem now is that PGMEA also dissolves the photoresist (AZ-5214) used in the liftoff process. Experiments with using different solvents to be able to dissolve IP-Dip or IPS which does not dissolve AZ-5214 turned out to be unsuccessful.

Since the liftoff process turned out to be not feasible a different approach has been taken. In stead of using a liftoff process a shadow mask has been used, which only lets gold through in certain regions. A schematic representation of the process is depicted in figure 19 . Using a home made stage aligner the shadow mask is aligned with the chip underneath it. The chip with the mask

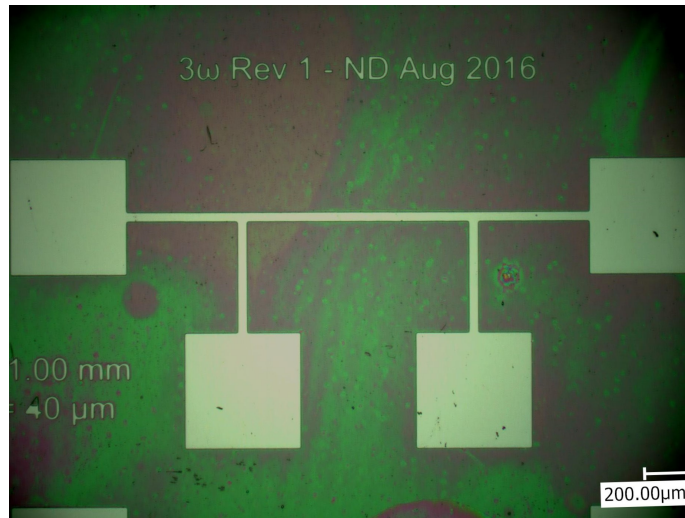


Figure 18: Optical image of photoresist spin coated onto a silicon chip where a pattern is dissolved by the aid of photo lithography (seen as colorless).

is then placed in a e-beam evaporator to deposit gold on top of the structure. To improve the adhesion of the gold on the silicon chip a seed layer of 5nm Titanium is deposited underneath.

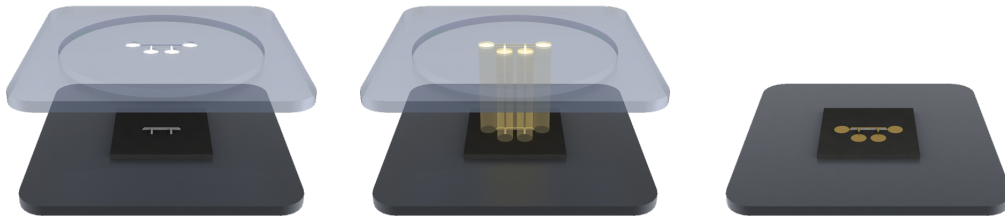


Figure 19: Schematic representation of the gold evaporation process using a shadow mask.

V. Microfabrication

It is essential for the experiment that the different pads are connected electronically through the gold lines. In figure 20 and SEM picture together with an EDS map of the side ramp of the device structure is depicted. What can be seen is that there is a continuous film of gold is on top of the structure, but that it is disconnected with the gold line on the bottom of the structure.

The way this disconnection is resolved is by locally depositing a layer of tungsten (W) using focused ion beam deposition (FID). See also figure 21 . With FID locally a precursor is flowed near the region of interest by an inserting a needle into the SEM. Just like in the other film deposition techniques the precursor used (tungstenhexacarbonyl) contains a tungsten atom surrounded by organic molecules (carbonyl groups). The precursor gets adsorbed onto the surface and at the places scanned by the focused ion beam it will dissociate leaving tungsten on the surface and the

The thermal properties of lightweight, strong and thermally insulating hierarchical nano materials.

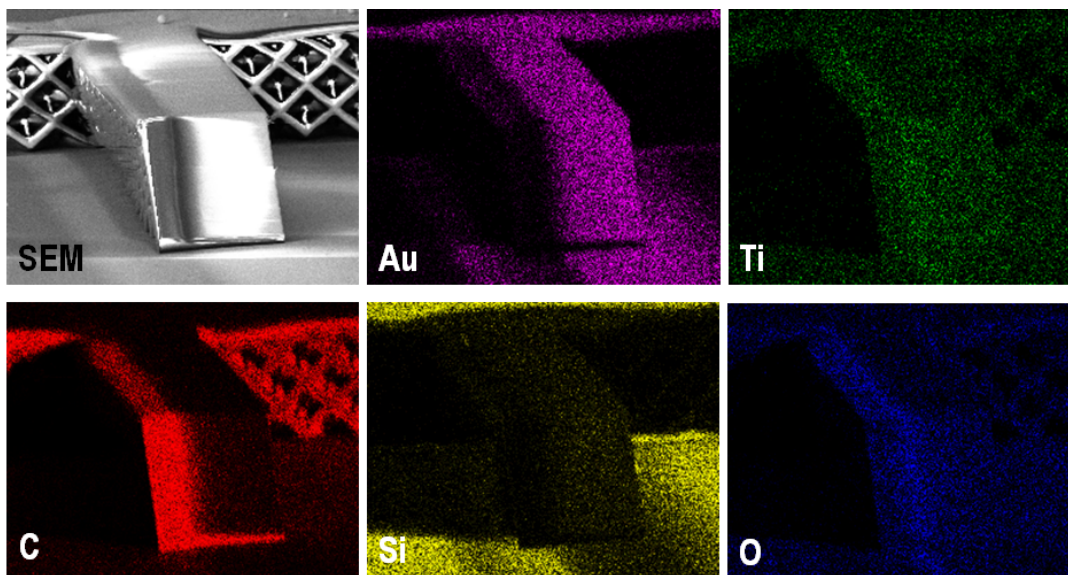


Figure 20: SEM pictures and EDS maps of gold (Au), titanium (Ti), carbon(C), silicon (Si), oxygen (O) of the side ramp of the device structure. Note that there is a shadow visible in the structure due to the location of the secondary electron detector.

carbonyl groups will get pumped away by the vacuum pump in the SEM chamber. The result before and after FID can be seen at figure 21 . The result is that the resistance between the pads dropped from one $M\Omega$ to hundred Ω .

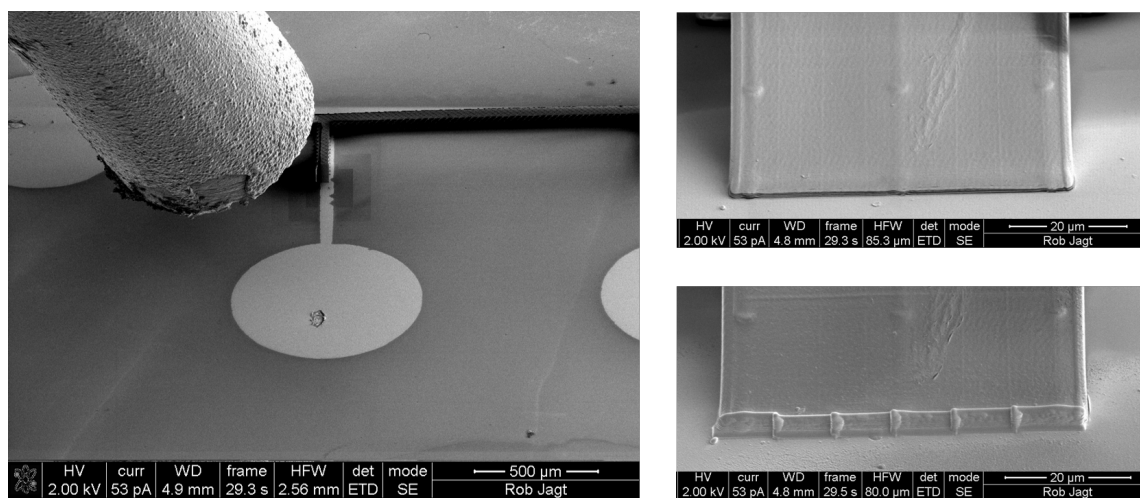


Figure 21: Example of focused ion beam deposition. Left: Needle inserted into SEM chamber to locally flow the tungsten precursor ($W[CO]_6$). Right: SEM pictures before(top) and after(bottom) focused ion beam deposition.

VI. Creating the top plate

The objective of the experiment is to determine the thermal conductivity of the nanolattice. Within the experiment it is important that the largest part of the temperature difference is over the nanolattice to obtain good sensitivity to changes in the thermal conductivity. In order to fulfill this requirement it is important that the thermal conductivity of the top plate is (much) larger than the thermal conductivity of the nanolattice. Next to this also the porosity of this top plate should be low, ideally not porous at all to make sure no gold gets on the structure.

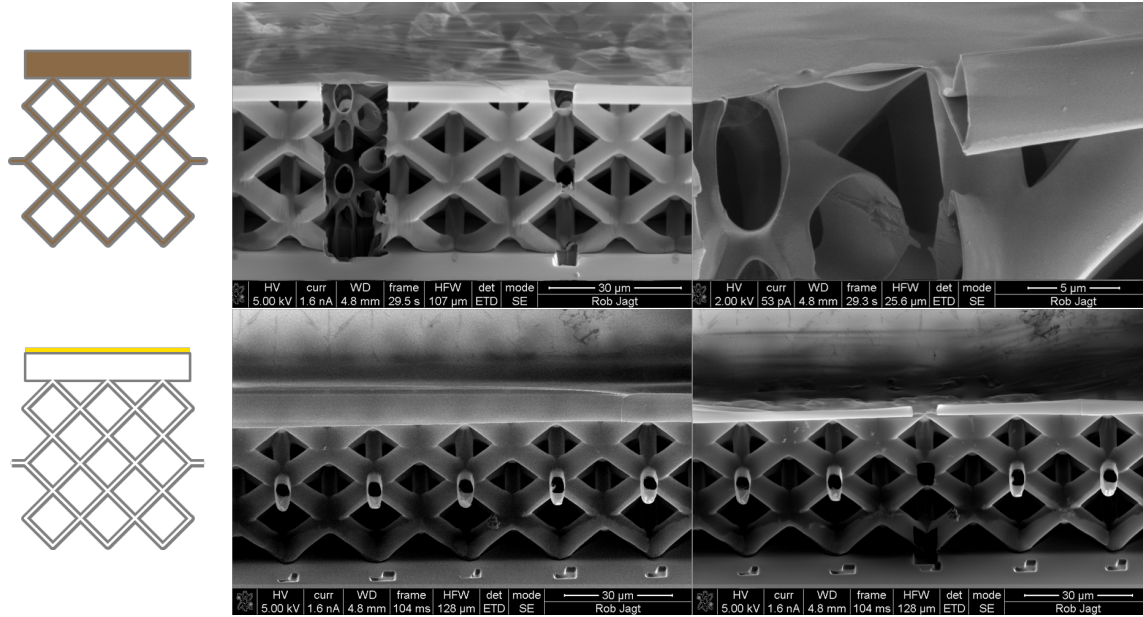


Figure 22: Left figures: schematic of a nanolattice before and after hollowing out the structure. Top figures: SEM pictures of the cross-section of a hollowed out structure (middle figure) and a close-up of the top of this structure (right figure). Bottom figures: SEM pictures before (middle figure) and after (right figure) making cross-sections using a focused ion beam.

The most straightforward way to write a non porous top plate is to simply write a solid plate. This works fine for the case of solid polymer nanolattices. However in the case of hollow nanolattices this creates a problem. To see this look at the left part of figure 22 . When the structure is hollowed out, writing a solid plate with polymer creates a hollow plate with no thermal path (except for the sides) from top to bottom. To circumvent this problem a different design has to be programmed such that after writing and hollowing out the structure there is a conductive path from top to bottom and the structure has minimum porosity.

Initially it was believed that the top plate will collapse due to the fact that top film of the top plate is only supported by a very thin layer and that the van der Waals bonding between the top and bottom film will cause the top film to fall down onto the other structure (see also the top figures of figure 22). However it was observed later that this layer collapse was induced by the focused ion beam. It is believed that due to the low electrical conductivity of the structure and the chip negative charge remains buried inside the structure. The focused ion beam uses positively charged gallium ions for imaging, which cause a large electrostatic force between the top and

bottom film causing it to come down. See also the bottom figures of figure 22 .

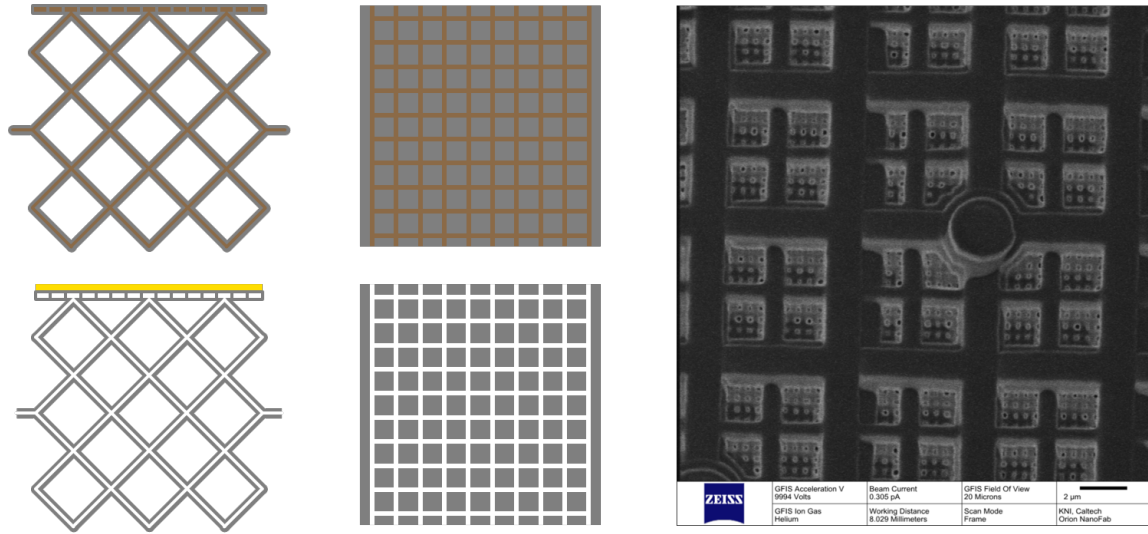


Figure 23: Left figures: schematic representation of the coated structure with the polymer still inside (top figures) and the hollowed out structure (bottom figures). Right figure: Helium ion microscope pictures of the top plate after coating it with alumina. Picture taken with the Zeiss Orion Nanofab helium ion microscope, courtesy of Matt Sullivan-Hunt.

The way in which this problem is solved is by writing a mesh in stead of a top plate. This is visualized in figure 23 . The top plate is replaced by a mesh of closely spaced lines which form a square lattice. The holes between the lines form a porous network. When the size of the holes is small enough then the empty space will be filled when the structure is coated using ALD. Then after the structure is hollowed out there will be a conductive pathway down, while at the same time the top plate is not porous.

To identify the correct settings to obtain a top plate with porous holes a parameter sweep for different parameters is done. The most important parameters governing the size of these holes are the hatching distance and the laser power. The laser power, LP , is a number between 0 and 100, which indicate the percentage of the maximum power used. The hatching distance, H , is the programmed distance between two lines. When the lines are placed to close to each other, or the used laser power is too high the lines will merge creating a patterned plate. On the contrary if the laser power is too low or the hatching distance too high the plate porosity will be unnecessary high.

The diameter of the hole is increasing with increasing hatching distance, while it is decreasing for increasing laser power. The higher laser power causes more initiators to become radicalized leading to more cross-linking and hence to larger polymer beams. This will reduce the space between two adjacent lines and hence the hole diameter.

An example of a measurement is depicted in the left side of figure 24 . The reason that the holes are circular instead of square is because of the proximity effects that the beams start to merge when brought together. For the entire parameter sweep the holes diameters are measured and are depicted in the table depicted on the right side of figure 24 . The smallest diameter measured was

80 nm, meaning that it is possible to create a plate which is solid when the coated film thickness is greater than 40 nm.

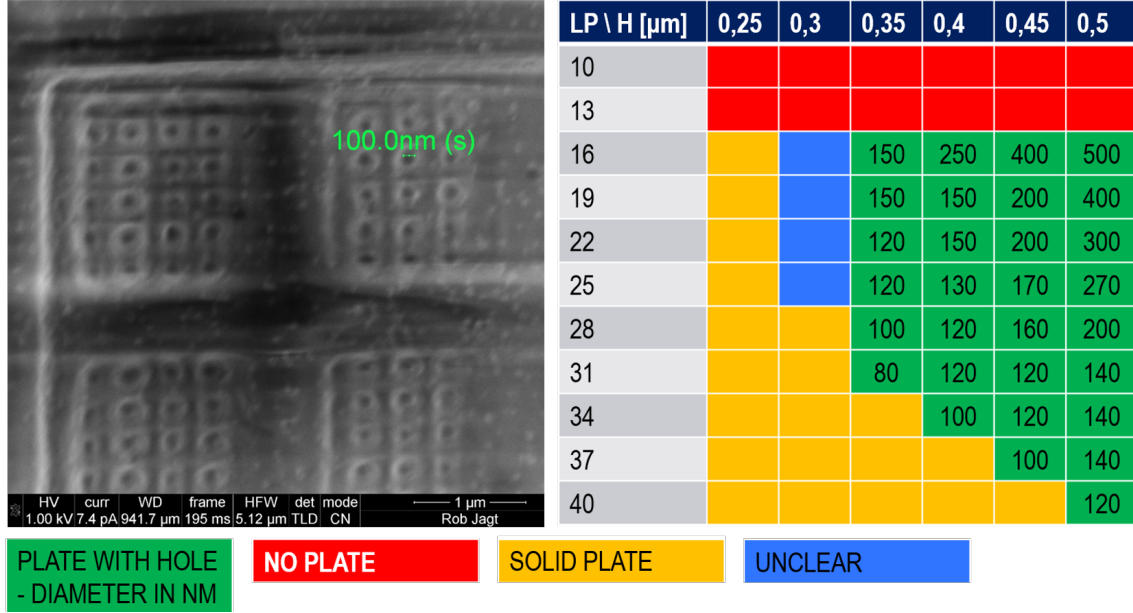


Figure 24: Left figure: SEM picture of the top plate, together with a measurement of the hole diameter. Picture taken using immersion mode. Right table: Table of the measured hole diameter for different values of laser power and hatching distance. Colors indicate the state of the mesh, numbers indicate the diameter of the hole in nm.

Note that the mesh does not only consist of parallel lines written as close as possible to each other, but that these lines are written into a larger meshes also consisting of square lattices. These lattices have a hatching distance of $6.25 \mu\text{m}$ and $3.125 \mu\text{m}$ and have larger radii than the fine mesh. The reason for doing this is that the weight of the top plate is carried by the larger meshes and that the fine mesh can be written with lower laser power without loss of structural integrity. To confirm that now the top plate indeed consists of two thin film with pillars connecting them cross-sections are made. An example of this is depicted in figure 25 .

VII. Final result

An optical image of the final result is depicted in figure 26 . The gold pads are connected to a chip holder through thin wires. These wires are bonded onto the gold pads and the chip by wirebonding, which uses mechanical vibrations to bond the wire to the surface. The blue color of the chip is due to the thin film of alumina (107 nm) on top of the silicon chip, which causes the blue light present in microscope light to interfere constructively. The chip is connected to the rest of the circuit as depicted in figure 13 . Additionally a thermocouple is placed on the chip to control the temperature of the silicon chip.

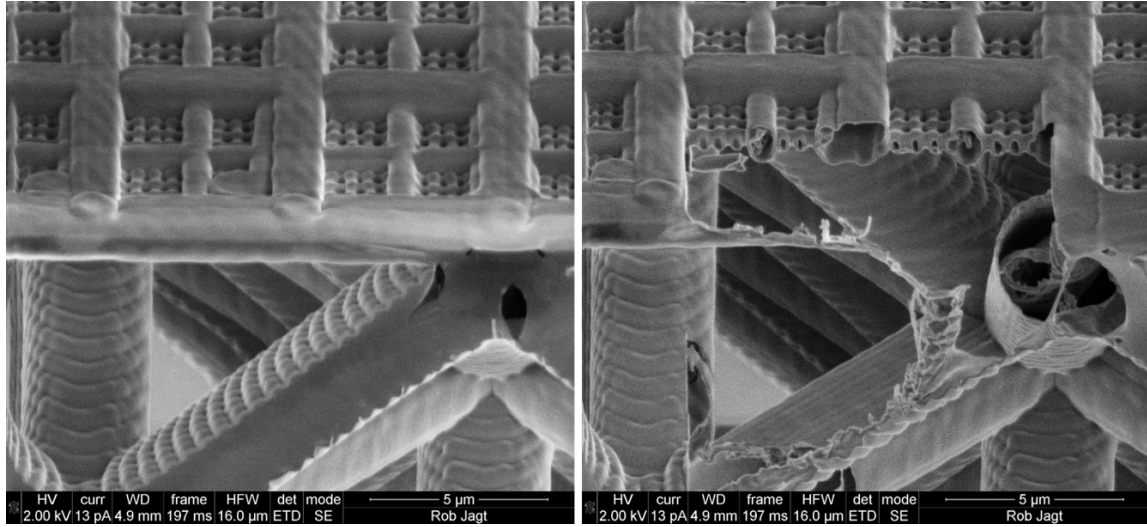


Figure 25: SEM pictures of the top plate with a written mesh before (left figure) a cleaning cross section have been made (right figure).

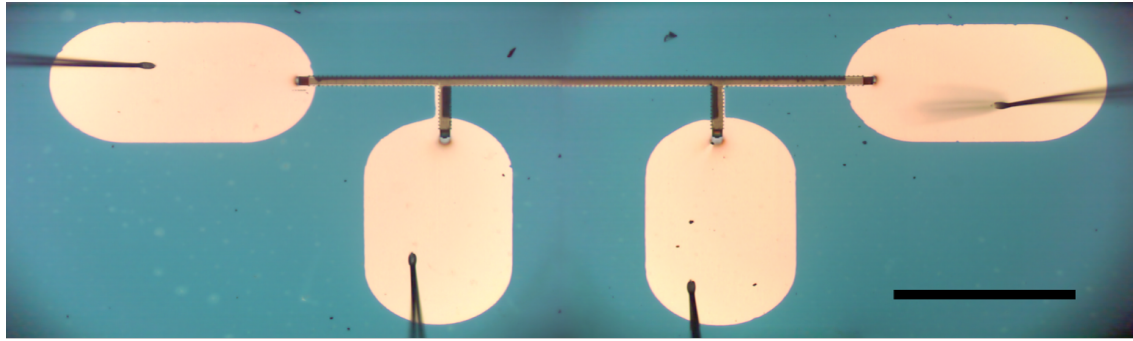


Figure 26: Optical images of the final device (hollow alumina with film thickness of 107 nm) close up (left figure) and on a chip (right figure). The black line at the right corner of the left figure indicates 1 mm.

V. RESULTS

Now that the fabrication process of the nanolattices have been discussed it is time to discuss the experimental results. First we will start of with a validation experiment on a glass substrate. Secondly the results for the thermal conductivity of the solid (polymer) nanolattices and the hollow (alumina / amorphous silicon) nanolattices will be presented. Finally this sections concludes with the mechanical data of alumina nanolattices. Note that in this section the data and theoretical fits only will presented. In the next section the results will be discussed in more detail.

I. Validation on Glass

In order to validate the experimental setup a validation experiment using gold on glass is used. To test this a test sample is made with simply a heating line on top of a glass substrate as depicted in figure 12 . As explained in the experimental section in order to cancel any influences of 3ω

currents flowing through the system the voltage drop measured across a resistor with similar resistance as the heater line is subtracted from the voltage drop over the heater line. This measured voltage together with the triggering signal is depicted in figure 27 . Here the signal is oscillating both at a frequency of 1ω and 3ω due to imperfect cancellations of the two signals. This is resolved by the analogue to digital converter. Discussions on possible sources of error and noise are dealt with in the next section.

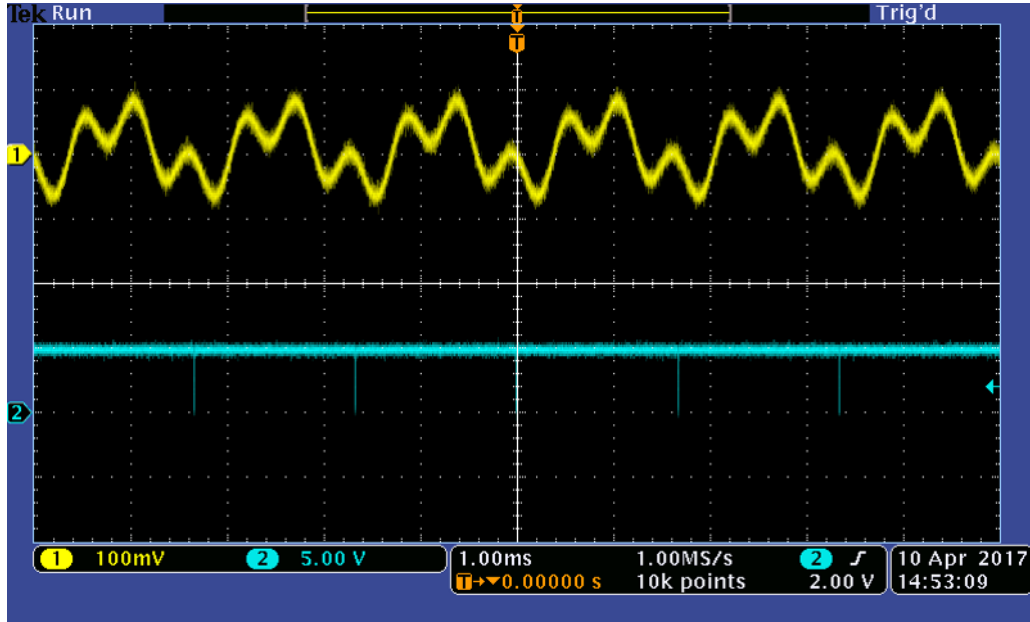


Figure 27: Oscilloscope image depicting the measured 3ω voltage (yellow) and the triggering signal (blue) versus time.

The measured temperature of the heater line with glass substrate for different driving frequencies is depicted in figure 28 . The model fit follows the same trends as the data and the fitted thermal conductivity value of 1.63 [W/mK] is close the literature value of 1.4 [W/mK].

II. Thermal conductivity of polymer nanolattices

Now that the experimental setup has been validated it is time to look at the data of the nanolattices made out of solid and hollow beams. The data together with the model fit and confidence interval for a nanolattice with solid polymer beams with a radius of $2\mu m$ is depicted in figure 29 .

The polymer used in this experiment is one of the two photoresins provided by nanoscribe, which has the abbreviation IPS. This photoresist has the characteristic that it enable you to write large structures with smooth features. It is however not usefull when you want to resolve very fine features. The thermal properties of this polymer are characterized separately using a spectroscopy technique called time-domain thermoreflectance (TDTR), which will be discussed in more detail in the next section.

Similar device architectures and measurements have been made of the same polymer (IPS), where the radius of the solid beams has been varied. Due to the change of the radii the solid fraction (the percentage of space occupied) also changes accordingly. The solid fraction is calculated

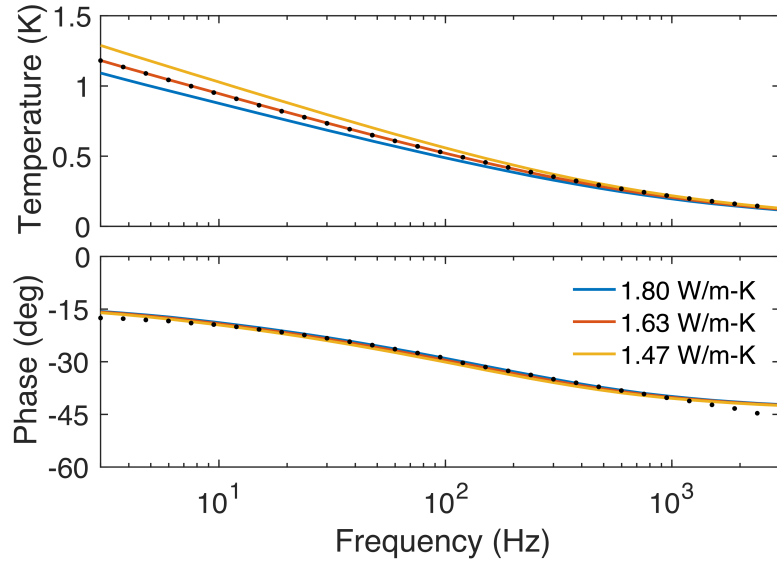


Figure 28: The measured absolute temperature of the gold heater line on top of the glass sample and corresponding phase together with the model fit for different driving frequencies.

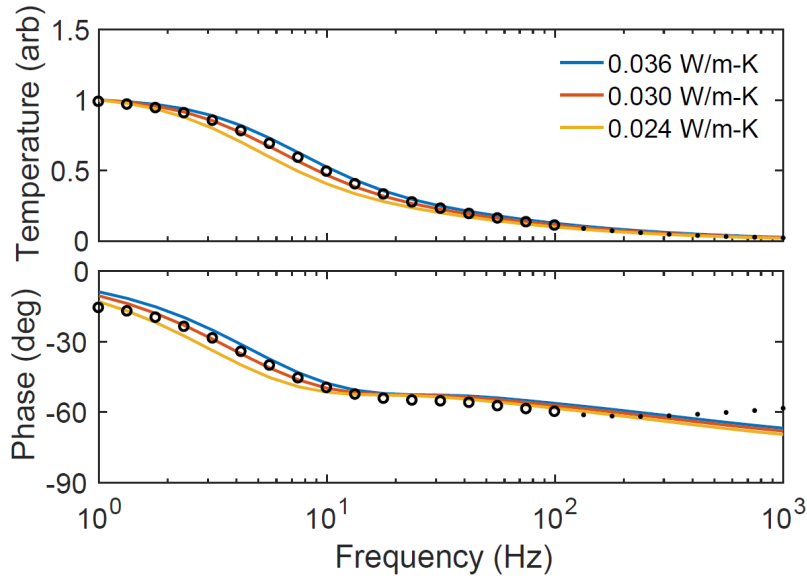


Figure 29: The measured absolute temperature of the gold heater line on top of the solid polymer nanolattice with a 2 μm beam radius and corresponding phase together with the model fit for different driving frequencies.

by using the CAD drawing of the unit cell and determine the occupied volume of the polymer and the volume of a unit cell. The solid fraction is then the ratio of the two. The fitted thermal conductivity as a function of the solid fraction together with the theoretical finite element results are depicted in figure 30 .

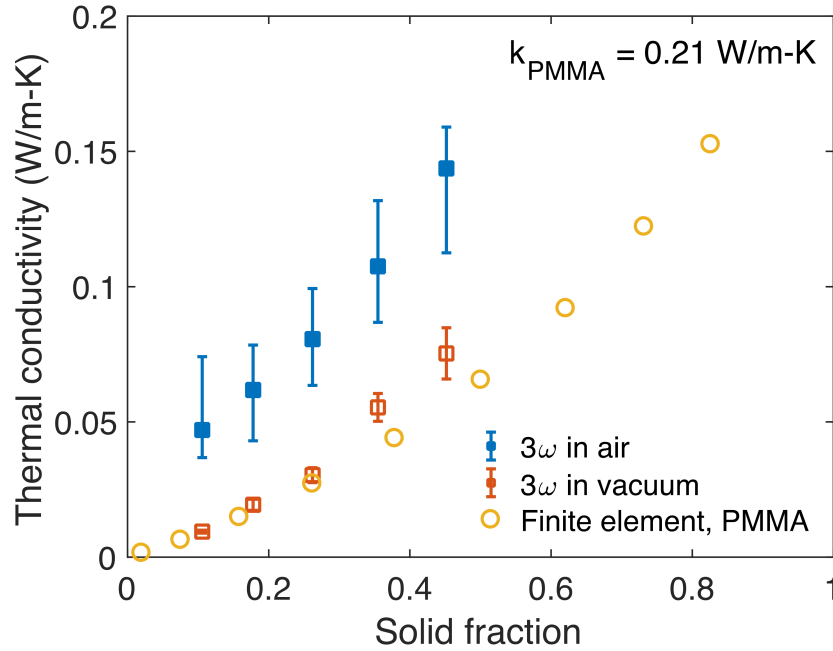


Figure 30: Fitted thermal conductivity of polymer nanolattice measured in air and in vacuum together with the simulated values (using a finite element model) as a function of solid fraction. Simulation and measurement are done for beam radius $r = 1.2, 1.6, 2.0, 2.4$ and 2.8 .

III. Thermal conductivity of alumina nanolattices

Following the fabrication procedure mentioned in the previous section also samples with hollow alumina nanolattices have been fabricated. Now the radius of the polymer scaffold is maintained at $2 \mu m$. Instead the wall thickness is varied from 22 nm to 169 nm. The temperature profile together with the data fit as a function of frequency is depicted in figure 31. The same data is acquired and analyzed in a similar manner for the other sample and these results are depicted in figure 32 .

IV. Thermal conductivity of silicon nanolattices

As for the hollow alumina lattices, for the hollow silicon nano lattices the radius of the polymer scaffold is maintained at $2 \mu m$ and the wall thickness is varied from 18 nm to a 192 nm. The results are depicted in figure 33 and 34 .

V. Mechanical properties of alumina nanolattices

Next to the thermal properties also the mechanical properties of the alumina nanolattices will be determined. Specifically the stiffness values will be estimated from the stress strain curves obtained from quasi static uniaxial compression experiments as is explained in the experimental section.

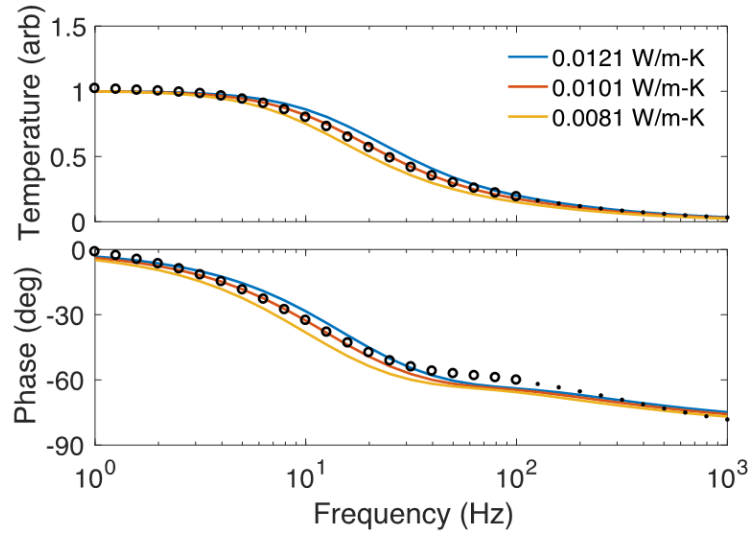


Figure 31: The measured absolute temperature of the gold heater line on top of the hollow alumina nanolattice and corresponding phase together with the model fit for different driving frequencies.

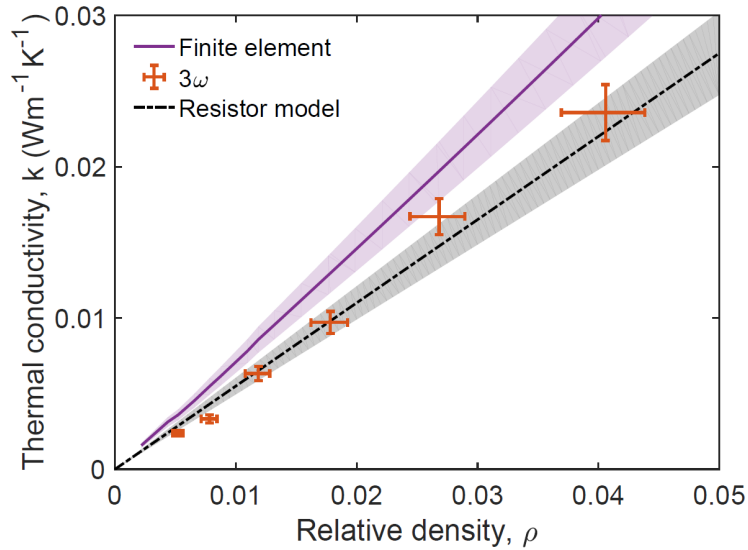


Figure 32: Fitted thermal conductivity of hollow alumina nanolattices measured in vacuum together with the simulated values (using a finite element model and an analytical approximation) as a function of solid fraction. Simulation and measurement are done for beam radius $r = 2$ with wall thickness $t = 22\text{nm}, 33\text{nm}, 50\text{nm}, 75\text{nm}, 112\text{nm}, 169\text{nm}$. The shaded bounds around the finite element and resistor model indicate the simulation results with 10% difference in bulk thermal conductivity.

The compression samples and the samples used for the thermal characterization are written on the same chip to ensure that both samples are created in similar conditions. The compression samples are made out of $5 \times 5 \times 5$ octet unit cells and an example of this is depicted in figure 35 . An example of the stress strain data of a uniaxial compression experiment is depicted in figure 36 .

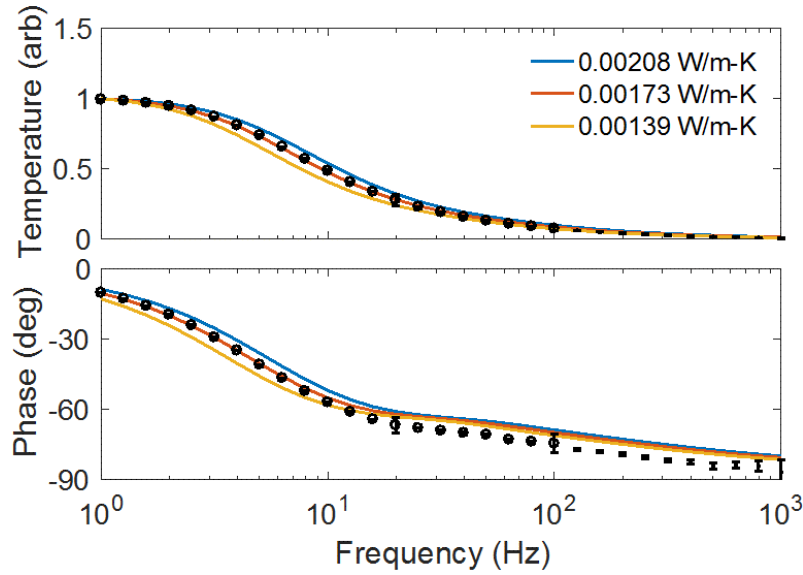


Figure 33: The measured absolute temperature of the gold heater line on top of the hollow silicon nanolattice and corresponding phase together with the model fit for different driving frequencies.

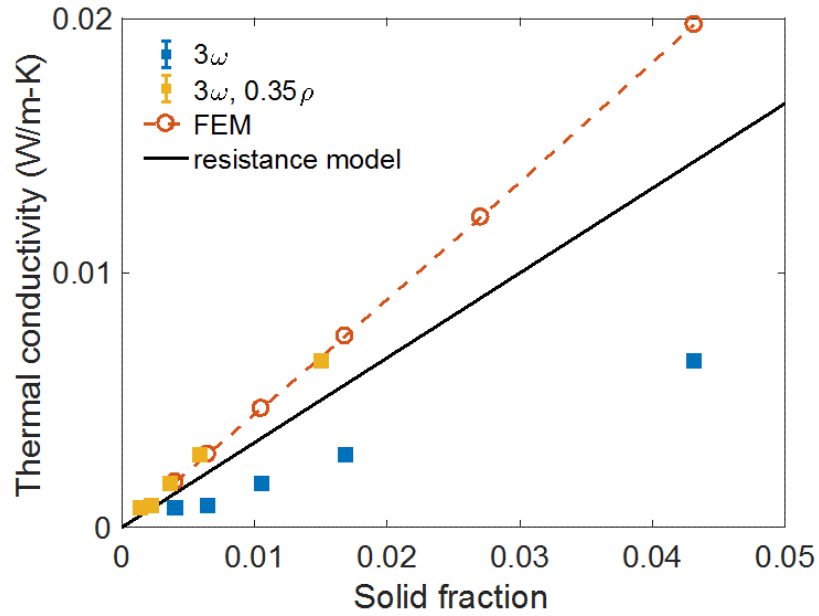


Figure 34: Fitted thermal conductivity of hollow silicon nanolattices measured in vacuum (for the measured density (blue) and 35% of the measured density (yellow)) together with the simulated values (using a finite element model and an analytical approximation) as a function of solid fraction. Simulation and measurement are done for beam radius $r = 2$ with wall thickness $t = 18\text{nm}, 29\text{nm}, 47\text{nm}, 75\text{nm}, 120\text{nm}, 192\text{nm}$.

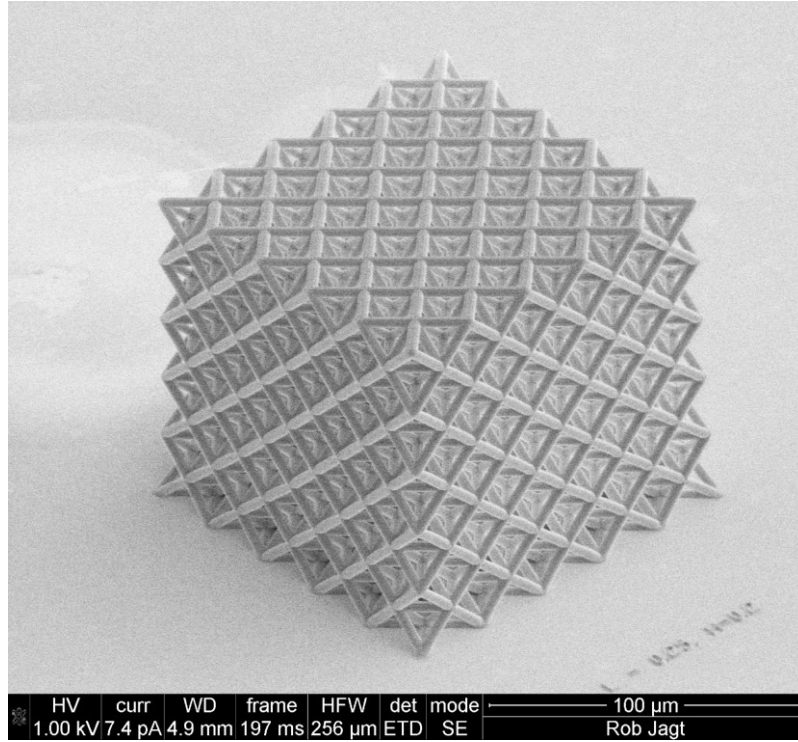


Figure 35: SEM picture of the compression sample used in the uniaxial compression experiments comprised of 125 octet unit cells ($5 \times 5 \times 5$) with a unit cell size of $25 \mu\text{m}$, beam radius of $2 \mu\text{m}$ and wall thickness of 112 nm .

This uniaxial compression test has been done for 6 different wall thicknesses, where the compression experiment has been repeated 3 times for each wall thickness. The results of these experiments together with the simulation results are depicted in figure 37 .

As described in the theory section it is possible to change the failure mechanism by changing the wall thickness to beam radius ratio. The stress strain data depicted in figure 36 is an example of a sample which failed in a catastrophic manner. It is initially strained elastically after which the nanolattice fractures. In figure 38 an example of an recoverable nanolattice is depicted. After being strained more than 30 % it almost fully recovers to its original shape.

VI. Multifunctional properties of alumina nanolattices

As explained previously it is the combined mechanical and thermal properties which make the hollow alumina nanolattices interesting. Therefore the specific modulus (stiffness divided by density) as a function of thermal conductivity is compared with a wide variety of other material classes in a eshelby type plot depicted in figure 39 .

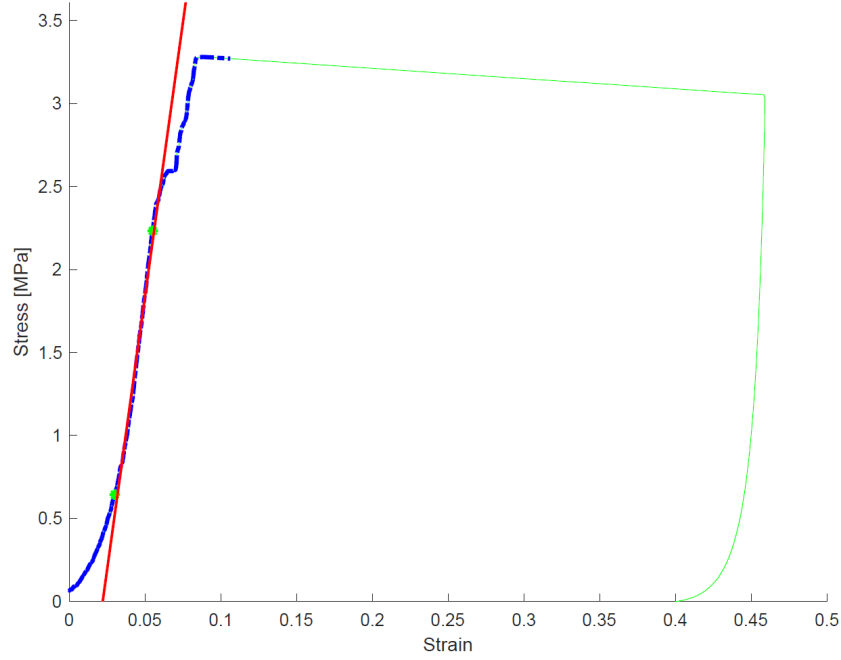


Figure 36: Stress strain data of a uniaxial compression of a hollow alumina nanolattice with a wall thickness of 112 nm.

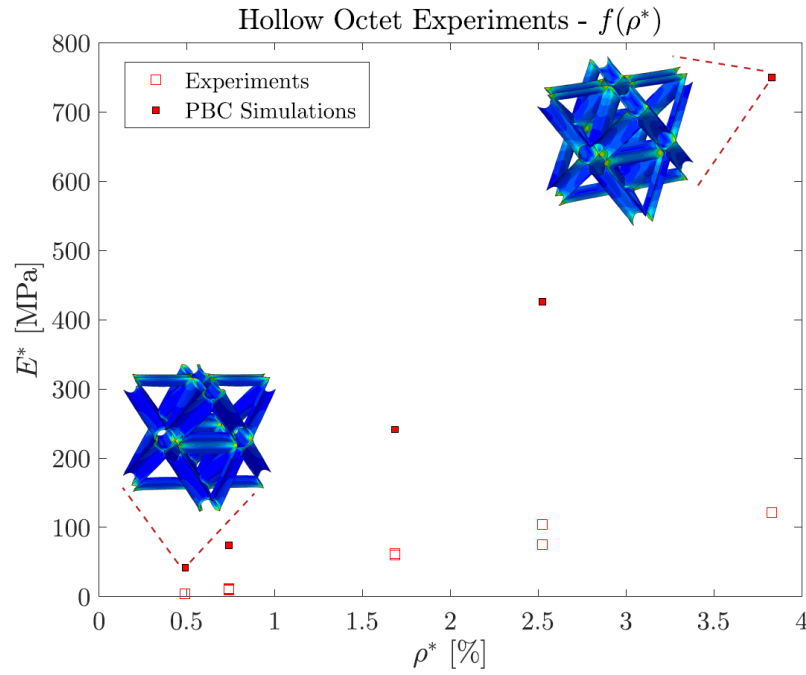


Figure 37: Experimental data and theoretical predictions of the stiffness values as a function of solid fraction. The theoretical values have been calculated using a finite element simulation with periodic boundary conditions. Simulations courtesy of Carlos Portela.

The thermal properties of lightweight, strong and thermally insulating hierarchical nano materials.

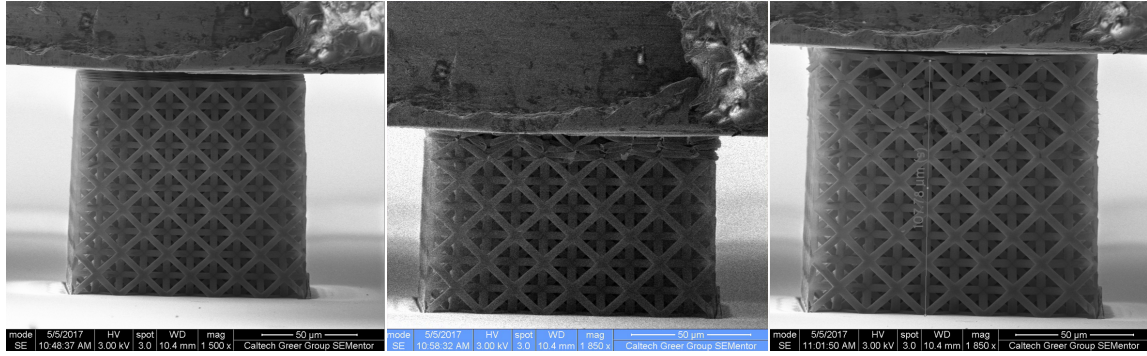


Figure 38: SEM pictures before(left), during (middle) and after the uniaxial compression of a nanolattice with a wall thickness of 22 nm. The nanolattice almost fully recovered to its original shape.

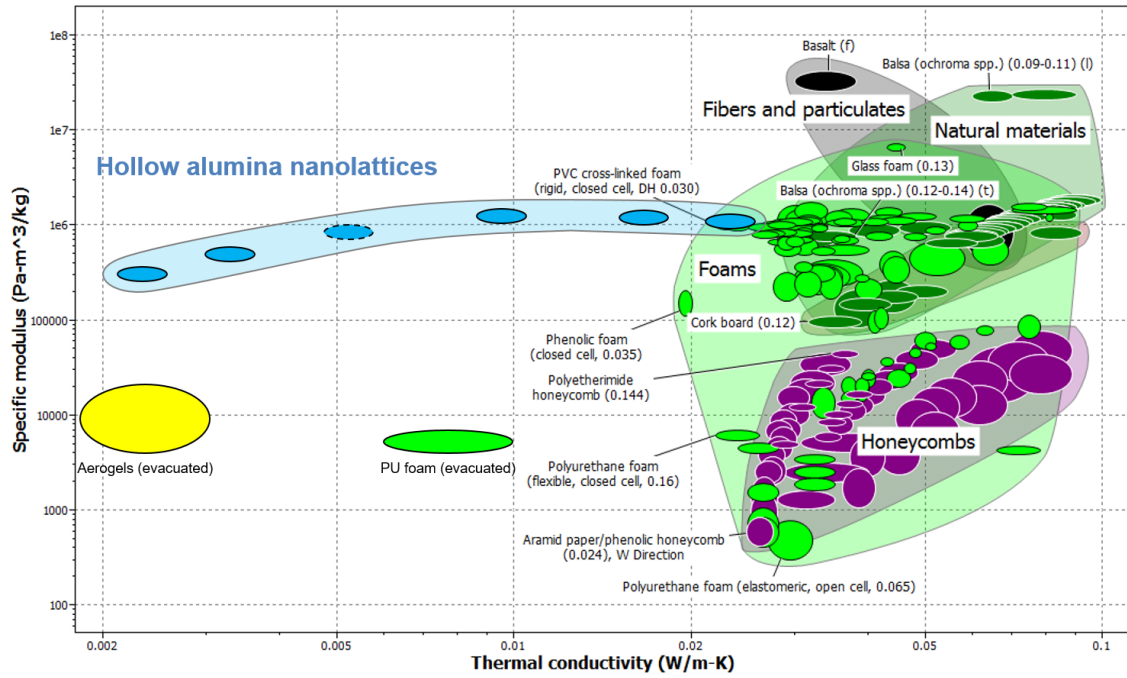


Figure 39: Plot indicating the specific modulus (stiffness divided by density) as a function of thermal conductivity for a wide variety of different materials. Plot generated with the help of Shi Luo.

VI. DISCUSSION

The results presented in the previous section will be compared with the theoretical predictions and the general validity of the results will be discussed. Specifically the breakdown of the 1D model assumption, the impact of stray capacitance/inductance on the measured signal, the results for amorphous silicon and whether it is expected to observe size effects and a qualitative description of the mechanical data will be discussed. Lastly the 3ω will be compared with other techniques to acquire thermal properties.

I. Breakdown of the 1D heat transport assumption

As described in the theory section in order to obtain analytical expressions for the heat transport through the nanolattices it is assumed that the heat flow through the top plate is one dimensional. However as can be seen in figure 40 formally this is not the case, because the heat flow has to go through the nodes where the nanolattice connects to the top plate. When the thermal conductivity of the top plate is higher than the nanolattice this effect can be neglected in steady state because the temperature drop over the top plate is much smaller than the total temperature drop with respect to the substrate. This is due to the higher thermal conductivity and the smaller distance the heat has to travel ($1\text{ }\mu\text{m}$ for the top plate versus $50\text{ }\mu\text{m}$ in the nanolattice). For the solid polymer nanolattice this requirement is satisfied since the top plate has a solid fraction of one. For the hollow nanolattices the mesh top plate has a solid fraction of a few percent which is still large enough when compared to the solid fraction of the nanolattice.

The above discussion indicates that the 1D assumption is valid in steady state. However within the 3ω experiment periodic heating is used. In this case another length scale needs to be taken into account, namely the thermal penetration depth. This length scale can be defined as,

$$L_p \equiv \left(\frac{\alpha}{2\omega} \right)^{1/2},$$

where α represents the thermal diffusivity and ω represents the frequency. The thermal penetration depth physically represents the distance a thermal wave travels over the period of the heat oscillation. For the solid polymer nanolattice at a frequency of 147 Hz this thermal penetration depth is only $25\text{ }\mu\text{m}$. At even higher frequencies this becomes even smaller. So at high frequency the 1D assumptions starts to break down and therefore the high frequency data point are omitted in the fitting procedure (this is indicated in the results figures by replacing the circles by points).

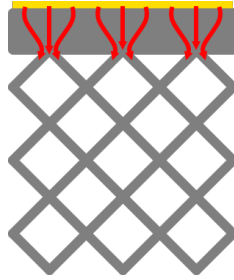


Figure 40: Schematic indicating the heat flow (indicated with red arrows) from the gold heater line (indicated with yellow) through the top plate to the nanolattice.

II. Influence of non-ideal electronics

As indicated in figure 12 the thermal properties are determined from measuring the voltage across the heater line at a frequency of 1ω and 3ω . Therefore it is important to investigate the non-ideal performance of the electronic components used in the circuit.

The first source of error is due to the current source. Next to the current at 1ω also higher harmonics will be present, including a current at 3ω causing a 3ω voltage. This will of course intervene with the measurements. As can be seen in figure 41 at low frequencies 0.01 % of the

signal provided by the current source is the higher harmonic at 3ω . As is indicated in the experimental setup in figure 13 these common three omega signals are compensated for by subtracting the measured voltage over a resistor from the voltage measured over the heater line.

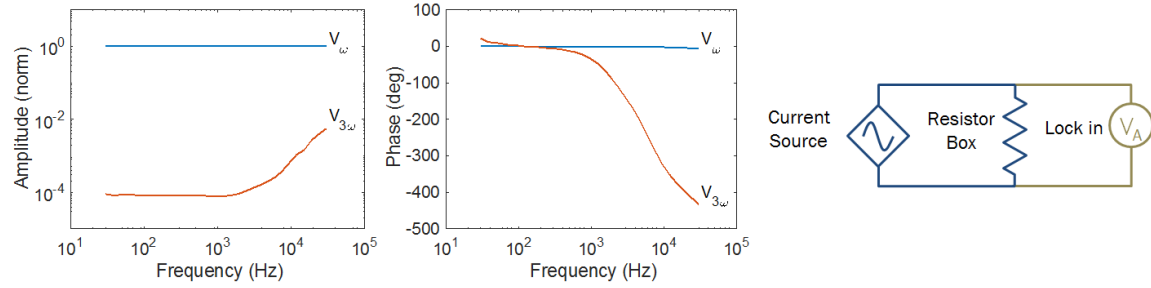


Figure 41: The normalized amplitude and phase of the voltage at 1ω and 3ω supplied by the current source as a function of the fundamental frequency. This voltage is measured by simply connecting the current source to the resistor box and measuring the response through the lock in amplifier.

What is essential in this line of reasoning is that there is no stray capacitance or inductance in the system. In order for the above mentioned signals to cancel it is important that the signals are perfectly in phase. Local stray capacitance could cause such a phase lag. Next to signals not being exactly in phase local loss of signal due to charge leaking because of such stray capacitance is another problem.

The problem with measuring these type of effects with the aid of a voltage or current source is that these sources have a internal feedback mechanism, compensating any decrease in potential in current. To understand this difference consider the schematic setup in figure 42 . Here a schematic drawing of the four point probe gold heater line on top of a glass substrate is depicted. A periodic current is supplied through the top and bottom pad, which as explained previously creates an 3ω voltage. This voltage is measured by the lock-in amplifier through the two right pads. Now imagine there is some stray capacitance within the circuit. The induced 3ω signal will start to charge this capacitor and the resulting current which will flow will cause a drop in the 3ω voltage over the heater line.

To see how this parallel capacitance may play a role consider the data in figure 42 . This is the measured 3ω signal of a sample with a gold heater line on top of a glass substrate with and without an additional capacitor of 180 nF parallel to the two probes. The transfer function, $H(s)$, relating the induced 3ω signal with the actual measured signal by the locking amplifier is given by

$$H(s) = \frac{1}{RCs + 1},$$

where $s = i\omega$, R is the resistance of the heater line and C is the capacitance.

As expected the measured signal is the most influenced at high frequencies. It is noticeable that even the data without any additional parallel capacitance resembles similar features at these higher frequencies. However it is not clear whether this is caused by parallel parasitic capacitance, by inductance of the wires. For the jumper wires used in the setup the skin effect could also be non negligible at 10 kHz. Finally it was observed that the cables were acting as antenna's picking

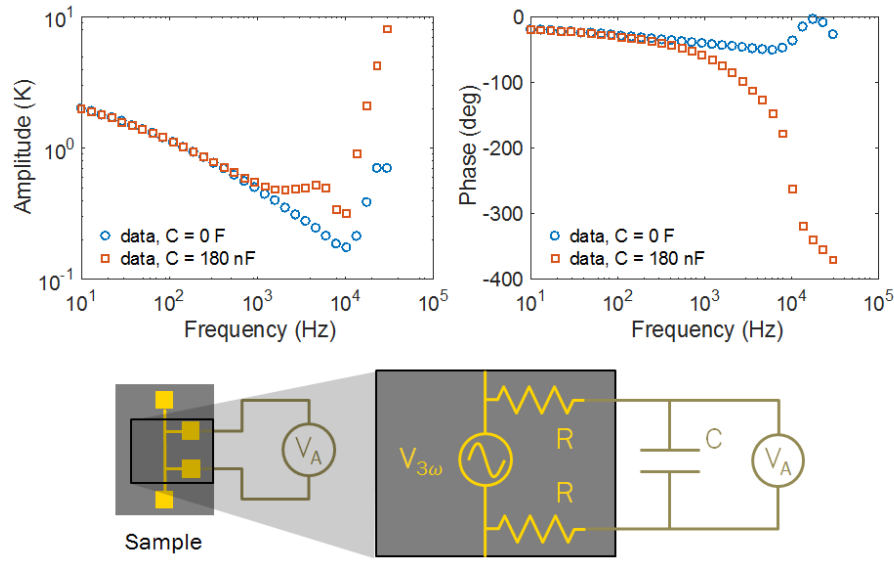


Figure 42: Top: The measured 3ω voltage (magnitude and phase) over a gold heater line on top of a glass substrate with no additional capacitance (blue) and an additional 180 nF capacitance (red). Bottom: schematic of the gold heater line and intrinsic resistance and capacitance.

up signal even though parts of the system were not connected.

Therefore to eliminate as much as possible of these type of sources of error most cables have been replaced with coaxial cables and the breadboard on which all the electronics are situated is replaced by a soldered circuit (see the supplementary for an precise schematic of the electronic network). Making these changes removed most of these problems and resulted in the experimental data for the different nanolattices and resembled the theoretical model relatively well. Still at very high frequency the measured phase lag was slightly larger, but it is unclear whether this is an measurement artifact or is the result of violation of the 1D heat transport assumption. However the impact of these data points on the final fitted value for the thermal conductivity is small.

So far the influence of non ideal electronic components were on the high frequency side of the measured spectrum. Also on the low frequency side electronic artifact are present. However in this case both the 1ω and 3ω signal are affected. Since for the temperature profile the quotient of $V_{3\omega}$ and V_{ω} is taken this effect can be compensated for. However since the 3ω signal is the third harmonic the 3ω signal at a frequency $\omega/3$ should be taken. This procedure is justified since the temperature signal for low frequencies (less then 1 Hz) is a flat function of frequency both in the magnitude and phase. An example of this is depicted in figure 43 . Since the temperatures are normalized and in this region the temperature profile is flat the effect in terms of measured thermal conductivity is very small. Being able to measure the temperature profile at these extreme low frequencies would enable to probe the thermal properties of larger structures or structures with even lower frequency.

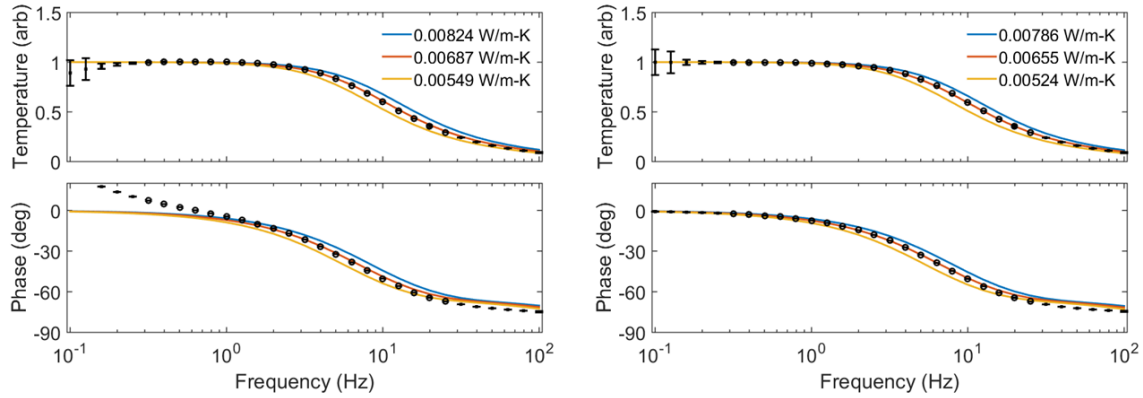


Figure 43: Measured absolute temperature and phase as a function of frequency uncompensated (left) and compensated (right).

III. Presence of size effects

The data for the solid polymer and hollow alumina nanolattice are in line with the finite element simulations and since no size effects are to be expected in these materials these results will not be discussed in depth. Instead the results for the hollow amorphous silicon nanolattices depicted in figure 33 and 34 will be discussed.

As can be seen in this figures the data can be well described by the analytical model, but the fitted thermal conductivity values lie below the theoretical predictions of the finite element model (all modeled with the same bulk thermal conductivity). When the device architecture is exactly as described in the sample fabrication section this could indicate that the seen difference between the finite element simulations and the fitted thermal conductivity values is due to the presence of size effects. However it is not certain that the film deposition of silicon by PECVD obtains similar quality films as ALD of alumina.

It is important that during film growth the growth conditions are good. Since the growth process is not self limiting unoptimized growth conditions could lead to poor or uncontrolled film growth. Due to safety constrains (SiH_4 is highly flammable) the precursor could only contain 10 wt% SiH_4 . This leads to less conformal coatings. Additionally the PECVD process is run at 250°C, which causes the polymer scaffold to out-gas during film growth leading to uncontrolled film growth. This problem is solved by placing the samples for several hours on a hotplate at 250 °C in a glovebox with an argon environment to prevent the polymer samples from burning.

To investigate the final as fabricated device architecture consider figure 44 . As can be seen in the overview picture of the device during the film growth no uncontrolled film growth due to out gassing took place. In the right part of figure 44 the top view of a compression samples is depicted, together with a cross section view of the hollow beams of the top of the compression sample. Visual inspection of the wall thickness of the hollow beams does not indicate a large anisotropy. However the charging of the hollow beams is too large for a reliable measurement of the wall thickness by SEM.

Instead a stainless steel disk is added in the PECVD vacuum chamber during silicon deposition. The thickness of the amorphous silicon layer is measured by depositing a protective layer of Pt

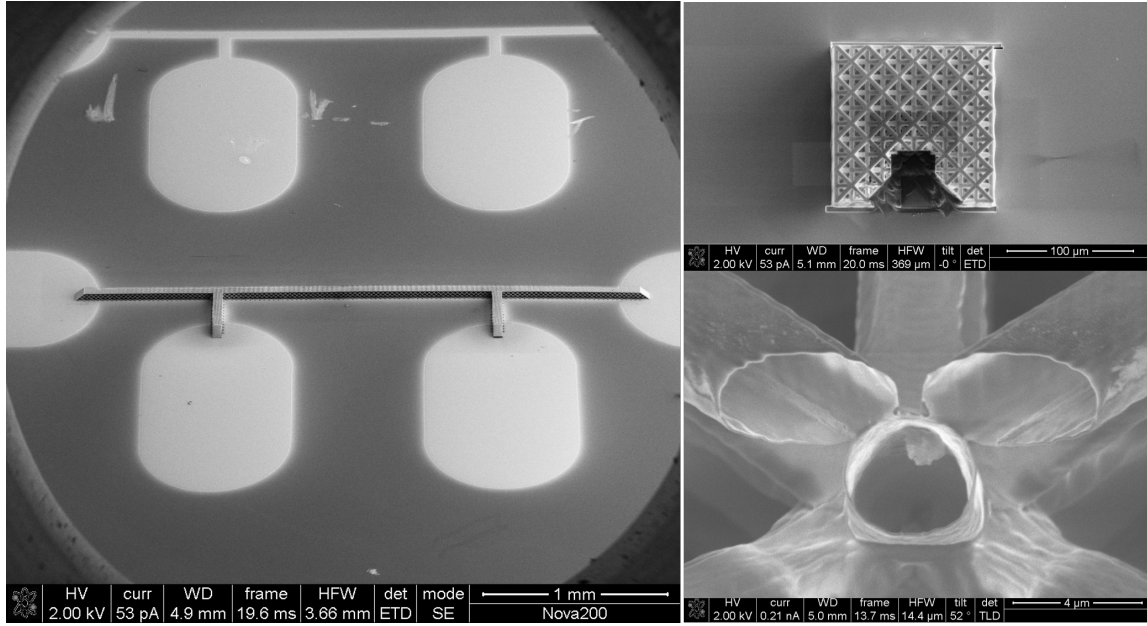


Figure 44: Left: SEM picture of as fabricated device consisting of hollow silicon nanolattices with a wall thickness of 47 nm. Right: SEM pictures of the compression sample top view (top) and zoomed in cross section view of the top beams (bottom).

using focused ion beam deposition, making a cross section by focused ion beam and measuring the thickness by SEM (see also figure 45). The measured thickness of 195 nm is close to the set thickness of 190 nm. Also the color of the steel disk was homogeneous throughout the steel disk indicating an uniform and flat surface. The problem however is that it is not guaranteed that the deposition rate onto the structure is similar onto the nanolattice. In fact in current research on using amorphous silicon nanolattices as anodes for battery applications indicate that the wall thickness inside the structures can be several times thinner on the inside of the structure than on the outside.

As is indicated in figure 34 the fit of the thermal data is repeated, but now with a density equal to 35% of the density expected based on the set film thickness. Now all the data points lie on the finite element results, which would indicate that there are no size effects present in these type of materials. If the hypothesis that the solid fraction is indeed much lower this would imply that the film thicknesses for the investigated samples are all below a 100 nm on average. As is indicated in figure 7 this would mean that no size effects are to be expected because the thermal transport is dominated by diffusions. However since no measurements of the actual achieved film thickness on the hollow nanolattices this hypothesis cannot be checked.

To convincingly show the presence of size effects the current measurements should be extended with samples with film thicknesses up to 1 or 2 μm and the film thicknesses should be measured with high enough accuracy to convincingly show the presence of size effects. Another procedure would be to investigate the possibility to heat treat the nanolattices to crystallize the amorphous silicon such that the thermal conductivity as a function of phonon mean free path changes.

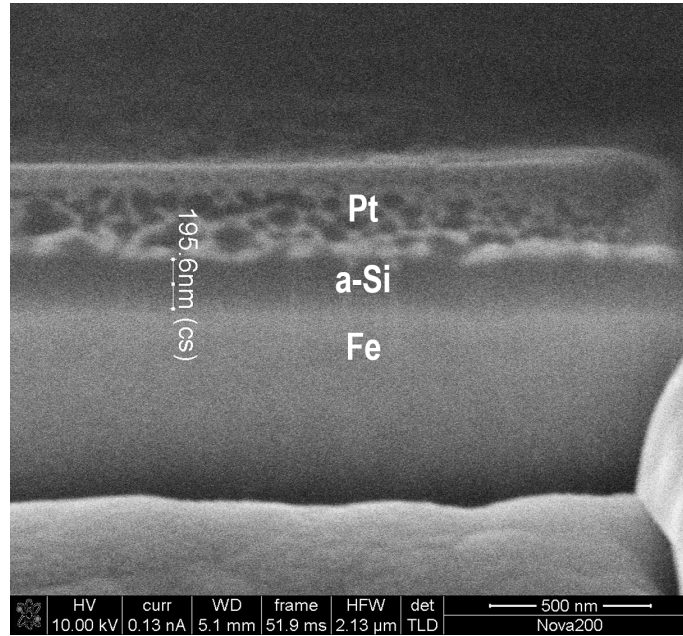


Figure 45: Cross section view of a stainless steel disk with a 190 nm (programmed) amorphous silicon layer deposited with PECVD. In order to protect the amorphous silicon layer a layer of Pt is locally deposited using focused ion beam deposition. The measured film thickness is approximately 195 nm.

IV. Discussion on the mechanical data

Next to the thermal properties also the mechanical properties of the hollow alumina samples have been determined. As can be seen in figure 37 the measured stiffness falls below the simulated stiffness modeled by finite elements. However the results are comparable with the results previously obtained by Meza et al 7 . The stiffness obtained here for octet alumina nanolattices with similar solid fractions were similar or slightly smaller than previously reported for similar solid fractions. This is due to the fact that the mechanical properties of nanolattice have a complex parameter space and depend on more than the solid fraction alone. As is indicated in figure 11 the structure here have relatively high beam radius to beam length ratio's leading to higher stress concentrations at the nodes, which leads to lower stiffness values.

The large difference between the simulations and the measured mechanical properties has to do with the discrepancy between the used model architecture and the as fabricated samples. First of all the simulations assuming periodic boundary conditions, effectively assuming the nanolattice extends into infinity in the lateral dimensions. However our compression samples only consists of $5 \times 5 \times 5$ unit cells. Secondly the ALD chamber could be contaminated causing poor film growth and therefore less favorable mechanical properties. Lastly the as fabricated sample is not exactly the same as the modeled device. Consider figure 25 . The layer by layer fabrication of the nanolattices is clearly apparent in the layered structure of the hollow beams. This waviness can be neglected in the modeling of the thermal properties, but can have a detrimental effect on the mechanical properties.

As depicted in figure 38 the hollow alumina nanolattices showed recoverable behavior when the

the wall thickness over beam radius was below a certain value. This was explained in the theory section by the fact that the stress levels in the nanolattice are such that the stress necessary to initiate local shell or beam buckling is below the critical stress required for fracture. The SEM images in figure 38 of the compression samples after deformation revealed localized cracking on and around the nodes, implying that the ALD alumina remained brittle and that the observed deformability and recoverability emerged from structural effects.

V. Other methods to determine the thermal conductivity

In this research the thermal conductivity has been determined using the 3ω method. However within the thermal sciences field different techniques exists to determine the thermal properties of materials. In this subsection a few comments will be made why in this case for the 3ω method has been chosen. Most techniques all rely on determining the transfer function, H , which relates a known heating signal Q to the measured temperature response ΔT ,

$$\Delta T = H Q,$$

where equation 3 is an example of how this would look like in the case for the 3ω experiment.

For example one could supply a known fixed heating signal and measure the steady state temperature rise. This is basically what is done in the 3ω experiments when the driving frequency is low such that the heat signal and temperature signal are effectively in phase. Then the heat equations boil down to Fouriers law and the thermal conductivity could be easily determined from the temperature rise.

Another well known procedure to determine the thermal properties of materials is by transient domain thermal reflectance (TDTR). This technique is a spectroscopic pump probe method where a known heat pulse is supplied by a laser pulse and the temperature decay is probed by another weaker laser pulse. This probing is done by coating the material with a thin layer of aluminum. Then the temperature is determined by making use of the temperature dependence of the reflectance of aluminum. Measuring this reflectance is then a probe for the temperature decay and the thermal properties can then be determined by fitting a thermal model to this experimental data.

Even though this is a well established technique there is a fundamental problem with this method when it comes to probing the thermal properties of nanolattices. The frequencies of the laser pulses used in TDTR measurements lie in the MHz range. This implies that the thermal penetration depth of TDTR is less than the typical unit cell size of a nanolattice, which would lead to poor experimental sensitivity to the thermal conductivity of the nanolattice. The frequency range used in the 3ω experiment is in the kHz range and below, giving rise to longer penetration depths and is therefore much more suitable to probe large structures with very low thermal conductivity.

VII. FUTURE WORK

In this research the concept of architecture in materials design has been used to alter the properties of materials. In this section a few remarks will be made on possible future steps, which can be taken with the knowledge obtained. Two matters will be discussed: using the concept of architecture to alter the thermal and mechanical properties of materials and using nano engineering to

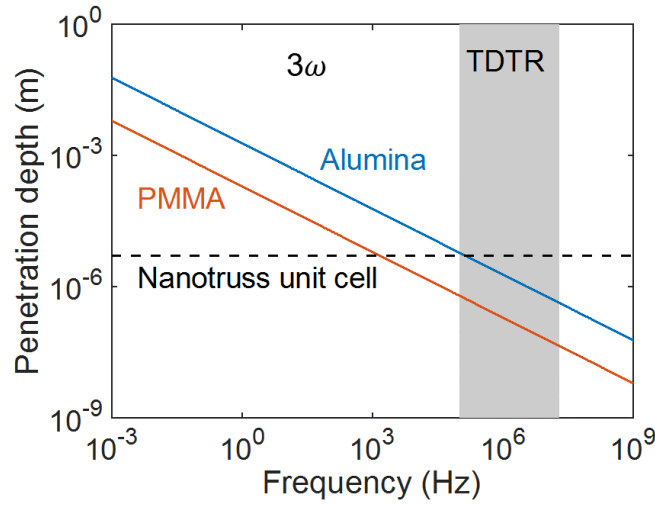


Figure 46: The thermal penetration depth of alumina (blue) and PMMA (orange) as a function of frequency. The region in grey indicate the frequency ranges used in TDTR. The frequency ranges used in the 3ω experiment are typically from 1 Hz until 10 kHz.

obtain more efficient thermal electric materials.

I. Using the concept of architecture to alter material properties

Until now the concept of architecture did not play a dominant role in this research and the architecture has been taken constant throughout. However it should be noted that the architecture is something which is programmed by the material scientist and the direct laser writing process allows for any complex or arbitrary structure to be made. It is not the scope of this thesis to go into depth in these types of questions, but just to give a flavor of the possibilities consider the two different architectures depicted in figure 47 .

Both architecture have the same solid fraction could be made out of the material and still have different material properties. For example due to the difference in directionality the thermal conductivity of the left architecture will be higher than for the right architecture, because heat can travel a shorter path in the former case than in the latter case. For the mechanical stiffness the directionality leads to a higher stiffness for the left architecture in the case that it is compressed from the top and vice versa for the right architecture. The point is that the architecture is controlled by the material scientist and that depending on the application at hand you can easily change it depending on the specific application at hand. Therefore formally it is not possible to tabulate the thermal or mechanical properties of nano architected materials as a function of for example solid fraction and the used material properties. Instead the material properties are defined by a complex function with the architecture being one of the arguments.

II. Decoupling thermal and other material properties

It is not the extreme low thermal conductivity which is a property only found in nano architected materials. Similar thermal conductivity values have been reported for materials like aerogels.

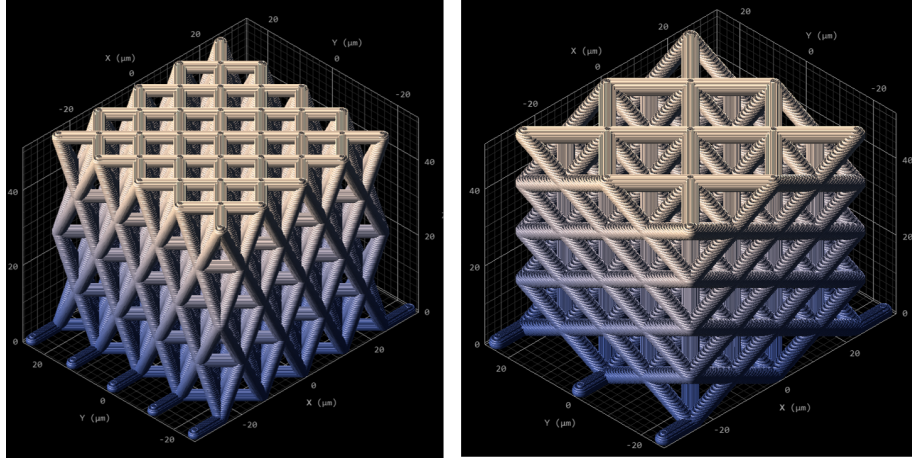


Figure 47: CAD drawings examples of a sample consisting of a octet unit cell with a base of $12,5\mu\text{m}$ by $12,5\mu\text{m}$ and a height of $25\mu\text{m}$ (left) and having a octet unit cell with a base of $25\mu\text{m}$ by $25\mu\text{m}$ and a height of $12,5\mu\text{m}$.

What is special about nano architected materials is the combined effect of thermal and mechanical properties. The use of architecture in nanoarchitected material enables the independent manipulation of coupled physical attributes. As introduced in the introduction it is possible to decouple thermal from mechanical properties.

A similar well known fundamental coupling between the thermal and electrical properties exists. Most materials which have a high electrical conductivity also have a high thermal conductivity, like for instance metals. However materials with very low thermal conductivity are also known to have vary low thermal conductivity. Within the field of thermal electric materials one wants to create a material with very low thermal conductivity, but very high electrical conductivity.

Thermal electric materials are materials which can convert a temperature difference directly into electricity. The efficiency of this process is defined by the figure of merit ZT and is defined as

$$ZT = \frac{S^2 \sigma T}{k},$$

where S is the Seebeck coefficient, σ the electrical conductivity, T the temperature and k the thermal conductivity.

Many different routes have been taken in trying to make more efficient thermal electric materials 23 . It has been shown that the cross plane thermal conductivity in layered WSe_2 crystals can be reduced substantially due to confinement of the phonons in the different layers 24 . Here we will shortly discuss a route of how to use the concept of architecture to nano engineer thermal electric materials with enhanced properties.

The idea is as follows: instead of making a hollow nanolattice with a single wall the films are created by alternatively growing two different materials. As an example here we take Bi_2Te_3 and Sb_2Te_3 , both materials with well known thermal electric properties. Also consider figure 48 . Bi and Sb both lie in the same column of the periodic table, but they lie in different rows. Therefore due to the atomic mismatch the phonons inside the crystal will scatter at the interface

between two different layers therefore being confined to a single layer, reducing the the thermal conductivity. On the other hand because of the fact that *Be* and *Sb* both lie in the same table of the periodic table the electronic band structure of Bi_2Te_3 and Sb_2Te_3 will be pretty similar and the scattering of electrons between the interfaces will be much less than the scattering of phonons. This technique of nano engineering therefore enables the decoupling of the thermal and electrical conductivity.

To further increase the ZT values it is possible to embed nano particles into the structure. Because of the quantization the average difference between the energy of the electrons or holes with the fermi level will increase. This would increase the Seebeck coefficient and therefore the value of ZT .

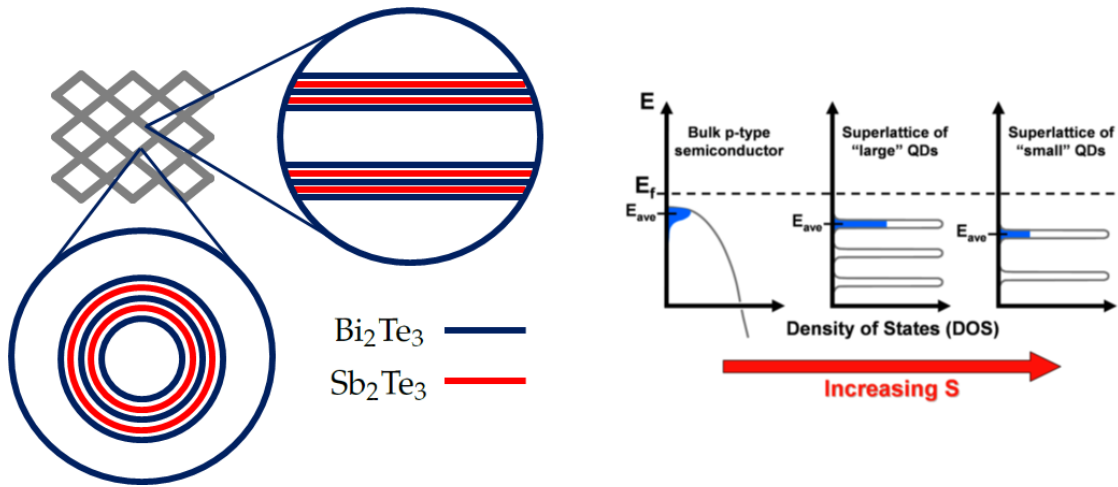


Figure 48: Left: Schematic drawing of a nanolattice with alternatively grown layers of Bi_2Te_3 and Sb_2Te_3 . Right: Schematic indicating the change in density of states for a bulk semiconductor, superlattice of large and small quantum dots.

VIII. CONCLUSIONS

In this research it has been shown that it is possible to create and characterize multifunctional meta materials which are extremely strong and simultaneously ultra lightweight and have very low thermal conductivity. This can be achieved by using the concept of architecture into the design of new materials. Because of the two photon lithography process used in the process it is possible to write structures smaller than the wavelength of the laser used to write the structures. The hierarchy of length scales that define the nanolattices span several orders of magnitudes. The final material has macroscopic dimensions of millimeters, unit cells with widths of tenths of micrometers, truss diameters of several micro meters and wall thicknesses of tens of nanometers. Because of this hierarchy of length scales it is possible to harness effects only present at the small scales such as improved strength 3 25 , flaw tolerance 26, and enhanced ductility 27 28 and a reduction in thermal conductivity 13 .

The thermal conductivity of solid polymer and hollow alumina / amorphous silicon nanolattices have been determined using a 3ω experiment. The fitted thermal conductivity values agreed with the simulated finite elements results for the solid polymer and hollow alumina samples. However a slight deviation has been found between simulations and experimental results for the amorphous silicon hollow nanolattices. It cannot be concluded whether this was due to the presence of classical size effects or whether the film growth was anisotropic leading to lower than simulated relative density.

Additionally the mechanical properties of the alumina samples have been determined using uniaxial compression experiments. The found stiffness values were comparable with previous research results, but were smaller than the finite element simulations with periodic boundary conditions. The difference between the experimental results and the simulations were attributed to imperfections caused by the layer by layer writing process used in direct laser writing. Even though the nanolattices were made out of intrinsically brittle alumina some nanolattices showed almost full recoverability after being strained more than 30% indicating mechanical resilience.

The use of architecture in nanoarchitected material enables the independent manipulation of coupled physical attributes and the development of materials with unprecedented capabilities. Ceramics have some of the highest strength- and stiffness-to-weight ratios of any material and have intrinsically low thermal conductivity, but are suboptimal for use as structural materials because of their brittleness and sensitivity to flaws. Here it is demonstrated that the creation of structural metamaterials composed of nanoscale ceramics can create materials which are simultaneously ultralight, strong, thermally insulating and mechanically resilient. It was shown that the multifunctional properties of the hollow alumina nanolattice showed an unique combination of high specific modulus and ultra low thermal conductivity. The measured thermal conductivity together with the thermal conductivity of low density silica aerogels are the lowest ever experimentally measured thermal conductivity. However the specific modulus is more than an order of magnitude higher.

It is therefore concluded that the thermal properties of nano lattices can be reliably measured using the described fabrication method and the 3ω experiment and that the hollow alumina nanolattices show unprecedented properties being lightweight, strong and lightweight and thermally insulating. These combined properties could turn out very useful for example for thermal protection systems in aerospace applications.

IX. SUPPLEMENTARY

Length measurements

The dimensions of the nanolattice are measured from SEM measurements. The height is determined to lie within $46\ \mu\text{m}$ and $49\ \mu\text{m}$. The width is determined to be between $49\ \mu\text{m}$ and $51\ \mu\text{m}$.

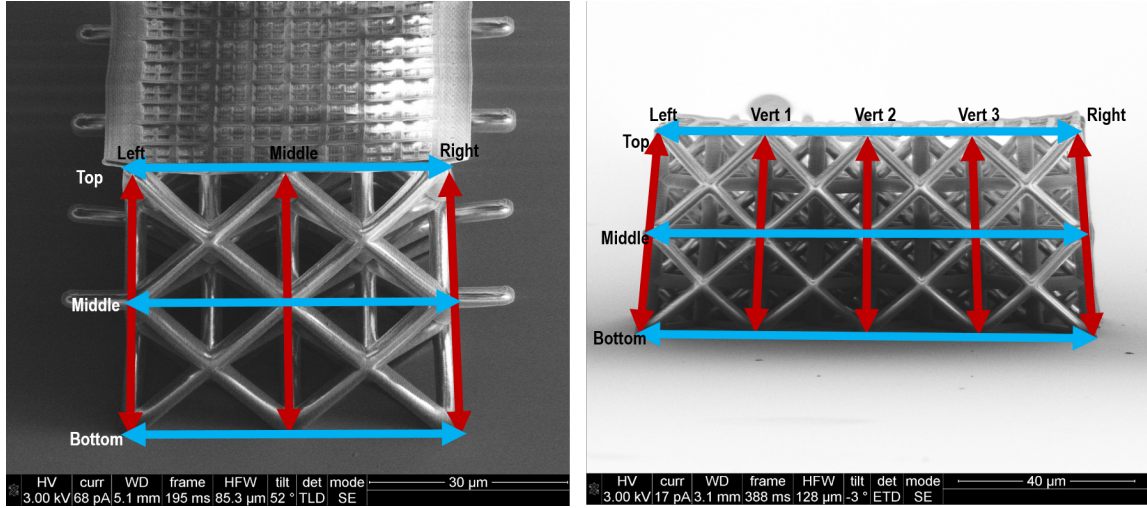


Figure 49: SEM pictures from a test sample to measure the height and width of the fabricated devices.

Bootstrapping results

The results for the bootstrapped fitted thermal conductivity values are depicted in figure 50 . As distributions for the height, width, solid fraction, heat capacity, beam radius and wall thickness

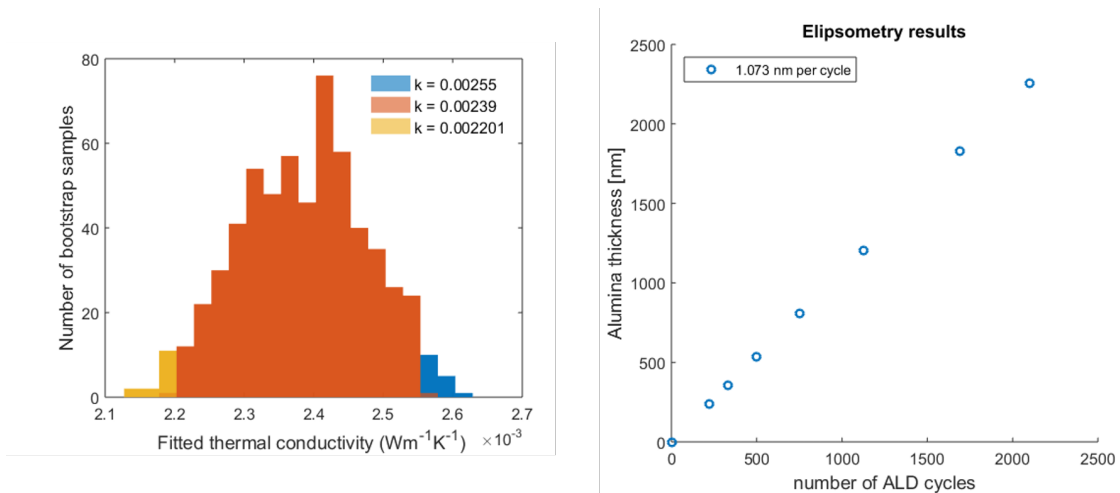


Figure 50: Left: Bootstrapping results of the fitted thermal conductivity values for an alumina nanolattice with wall thickness of $50\ \text{nm}$. Right: As measured alumina film thickness as a function of number of ALD cycles.

The thermal properties of lightweight, strong and thermally insulating hierarchical nano materials.

the triangular distribution is used with standard deviations that reflect the uncertainty in the variables. The wall thickness is checked using ellipsometry and the results are also depicted in figure 50 .

Compression video

Compression video: Octet22nm.avi

Electronics used in the 3 omega setup

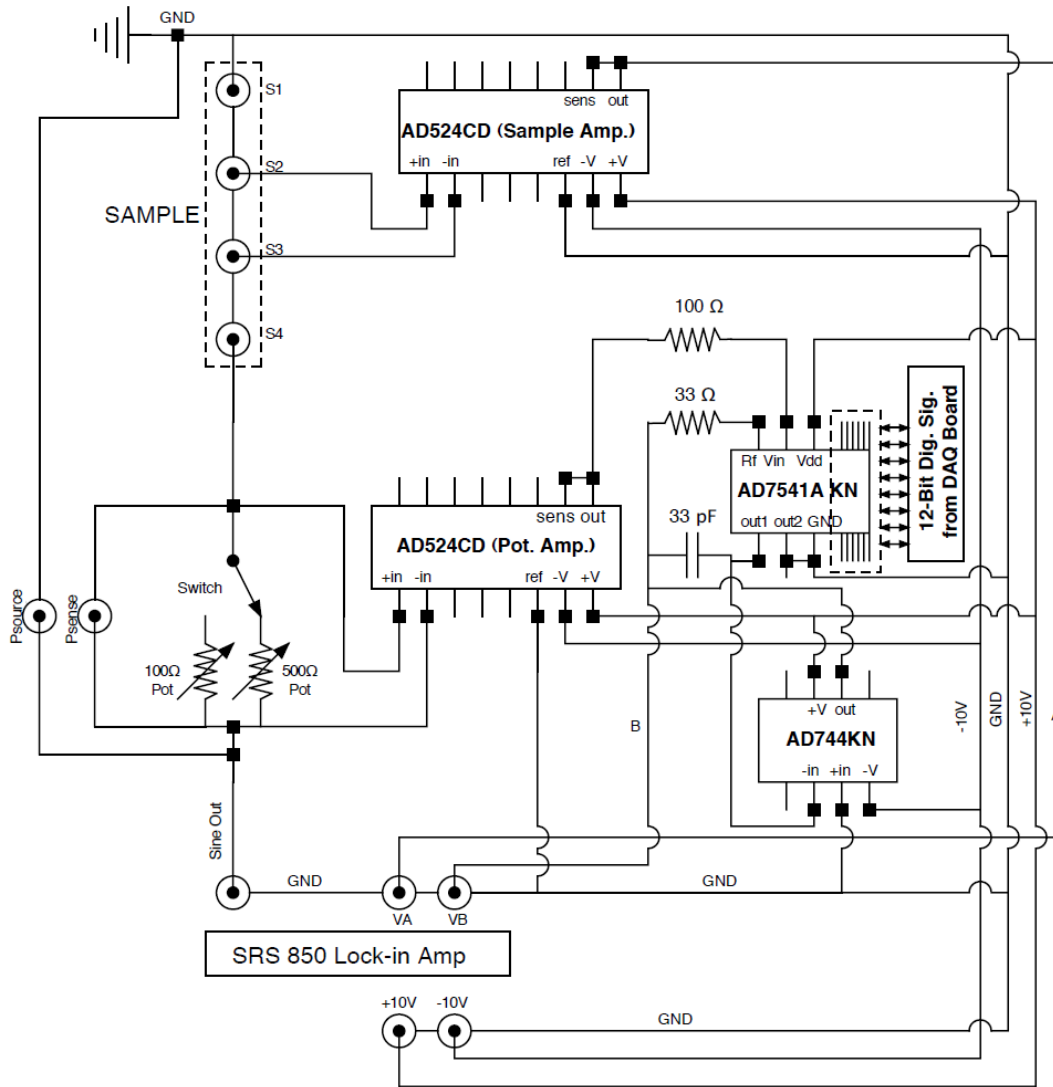


Figure 51: Electronic diagram indicating all components and connections used in the three omega experiment. Taken from 18 .

X. ACKNOWLEDGMENT

The author would like to thank the following people for their support: Alessandro Maggi, Ottman Tertuliano, Carlos Portella, Xiaoxing Xia, Shi Luo. Additionally the supervisors are thanked for their supervision: Prof. J.R.Greer, Prof A. Minnich and Prof. J.Th.M de Hosson. Lastly Nicholas Duo is thanked for the collaboration and nice research experience.

XI. REFERENCES

- [1] Lakes, Roderic. *Materials with structural hierarchy*. Nature 361.6412 (1993): 511-515.
- [2] Kim J-Y, Jang D, Greer JR. *Insights into deformation behavior and microstructure evolution in Nb single crystalline nanopillars under uniaxial tension and compression*. Scripta Materialia 61 (2009):300-3.
- [3] Greer, Julia R., and Jeff Th M. De Hosson. *Plasticity in small-sized metallic systems: Intrinsic versus extrinsic size effect*. Progress in Materials Science 56.6 (2011): 654-724.
- [4] Mille, Christian, Eric C. Tyrode, and Robert W. Corkery. *Inorganic chiral 3-D photonic crystals with bicontinuous gyroid structure replicated from butterfly wing scales*. Chemical Communications 47.35 (2011): 9873-9875.
- [5] Hamm, Christian E., et al. *Architecture and material properties of diatom shells provide effective mechanical protection*. Nature 421.6925 (2003): 841.
- [6] von Freymann, Georg, et al. *Bottom-up assembly of photonic crystals*. Chemical Society Reviews 42.7 (2013): 2528-2554.
- [7] Meza, Lucas R., Satyajit Das, and Julia R. Greer. *Strong, lightweight, and recoverable three-dimensional ceramic nanolattices*. Science 345.6202 (2014): 1322-1326.
- [8] Dou, Nicholas G., and Austin J. Minnich. *Heat conduction in multifunctional nanotrusses studied using Boltzmann transport equation*. Applied Physics Letters 108.1 (2016): 011902.
- [9] Schaedler, Tobias A., et al. *Ultralight metallic microlattices*. Science 334.6058 (2011): 962-965.
- [10] Olson, J. R., et al. *Thermal conductivity of diamond between 170 and 1200 K and the isotope effect*. Physical Review B 47.22 (1993): 14850.
- [11] Meza, Lucas R. *Design, Fabrication, and Mechanical Property Analysis of 3D Nanoarchitected Materials*. Diss. California Institute of Technology, 2016.
- [12] Chen, Gang. *Nanoscale energy transport and conversion*. Oxford university press (2005).
- [13] Kwon, Soonshin, et al. *Unusually High and Anisotropic Thermal Conductivity in Amorphous Silicon Nanostructures*. ACS nano 11.3 (2017): 2470-2476.
- [14] Shenogin, Sergei, et al. *Predicting the thermal conductivity of inorganic and polymeric glasses: The role of anharmonicity*. Journal of Applied Physics 105.3 (2009): 034906.
- [15] Borca-Tasciuc, T., A. R. Kumar, and G. Chen. *Data reduction in 3ω method for thin-film thermal conductivity determination*. Review of scientific instruments 72.4 (2001): 2139-2147.
- [16] H. S. Carslaw and J. C. Jaeger, *Conduction of Heat in Solids* Oxford University Press, 1959

- [17] MODEL SR830 DSP Lock-In Amplifier manual, Revision 2.5 (10/2011), Stanford Research Systems
- [18] Feser, Joseph Patrick. *Scalable routes to efficient thermoelectric materials*. (2010).
- [19] Deshpande, Vikram S., Norman A. Fleck, and Michael F. Ashby. *Effective properties of the octet-truss lattice material*. Journal of the Mechanics and Physics of Solids 49.8 (2001): 1747-1769.
- [20] Yee, Daryl W., et al. "Functionalized 3D Architected Materials via Thiol-Michael Addition and Two-Photon Lithography." Advanced Materials 29.16 (2017).
- [21] Cahill, David G. *Thermal conductivity measurement from 30 to 750 K: the 3ω method*. Review of scientific instruments 61.2 (1990): 802-808.
- [22] Anderson, P. W., B. I. Halperin, and C. M. Varma. *Anomalous low-temperature thermal properties of glasses and spin glasses*. Philosophical Magazine 25.1 (1972): 1-9.
- [23] Vineis, Christopher J., et al. *Nanostructured thermoelectrics: big efficiency gains from small features*. Advanced Materials 22.36 (2010): 3970-3980.
- [24] Chiritescu, Catalin, et al. "Ultralow thermal conductivity in disordered, layered WSe₂ crystals." Science 315.5810 (2007): 351-353.
- [25] Jang, Dongchan, et al. *Fabrication and deformation of three-dimensional hollow ceramic nanostructures*. Nature materials 12.10 (2013): 893-898.
- [26] Gu, X. Wendy, et al. *Microstructure versus flaw: mechanisms of failure and strength in nanostructures*. Nano letters 13.11 (2013): 5703-5709.
- [27] Chen, D. Z., et al. *Nanometallic glasses: size reduction brings ductility, surface state drives its extent*. Nano letters 13.9 (2013): 4462-4468.
- [28] Zheng, Xiaoyu, et al. *Multiscale metallic metamaterials*. Nature materials 15.10 (2016): 1100-1106.